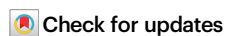





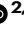


Infection-induced peripheral mitochondria fission drives ER encapsulations and inter-mitochondria contacts that rescue bioenergetics

Received: 6 February 2024

Accepted: 12 August 2024

Published online: 27 August 2024



William A. Hofstadter¹, Katelyn C. Cook ¹, Elene Tsopurashvili¹,
Robert Gebauer^{2,3}, Vojtěch Pražák ^{2,3}, Emily A. Machala ^{2,3}, Ji Woo Park¹,
Kay Grünewald ^{2,3}, Emmanuelle R. J. Quemini ^{2,3,4} & Ileana M. Cristea ¹✉

The dynamic regulation of mitochondria shape via fission and fusion is critical for cellular responses to stimuli. In homeostatic cells, two modes of mitochondrial fission, midzone and peripheral, provide a decision fork between either proliferation or clearance of mitochondria. However, the relationship between specific mitochondria shapes and functions remains unclear in many biological contexts. While commonly associated with decreased bioenergetics, fragmented mitochondria paradoxically exhibit elevated respiration in several disease states, including infection with the prevalent pathogen human cytomegalovirus (HCMV) and metastatic melanoma. Here, incorporating super-resolution microscopy with mass spectrometry and metabolic assays, we use HCMV infection to establish a molecular mechanism for maintaining respiration within a fragmented mitochondria population. We establish that HCMV induces fragmentation through peripheral mitochondrial fission coupled with suppression of mitochondria fusion. Unlike uninfected cells, the progeny of peripheral fission enter mitochondria-ER encapsulations (MENCs) where they are protected from degradation and bioenergetically stabilized during infection. MENCs also stabilize pro-viral inter-mitochondria contacts (IMCs), which electrochemically link mitochondria and promote respiration. Demonstrating a broader relevance, we show that the fragmented mitochondria within metastatic melanoma cells also form MENCs. Our findings establish a mechanism where mitochondria fragmentation can promote increased respiration, a feature relevant in the context of human diseases.

Subcellular organelles continually modulate their shapes in order to tune their functions. This is exemplified by mitochondria that undergo cycles of fission, fusion, and mitophagy^{1,2}. Each of these shape changes can have profound effects on the core mitochondrial functions of energy production, immune signaling, and cell death. Fused

mitochondria are generally found to be more bioenergetically active, while fragmented mitochondria are associated with oxidative stress and apoptosis^{3–6}. Emerging evidence shows that there are also distinct pathways of mitochondria fission that can differentially impact mitochondria function³. Fission can occur either at the midzone (inner 50%

of the mitochondria) or, as recently uncovered, at the periphery (outer 25% of each end), with the position of fission affecting the downstream fate of the progenies³. Unlike midzone fission, which promotes the proliferation of healthy mitochondria, the smaller progenies derived from peripheral fission were reported to exhibit lower bioenergetics and suggested to be targeted for degradation through mitophagy³. However, it remains unknown how the balance between these two modes of fission is regulated, as well as the pathogenic consequences of disrupting this balance.

Mitochondria shape is commonly regulated by pathogens, including viruses, to toggle the central processes that mitochondria regulate^{7,8}. For example, dengue virus promotes mitochondria fusion, resulting in increased mitochondria respiration⁹. Conversely, hepatitis C and B viruses (HCV and HBV) promote mitochondria fragmentation, resulting in decreased respiration^{10–12}. The ubiquitous β -herpesvirus human cytomegalovirus (HCMV), however, represents a paradox. HCMV infection induces significant mitochondria fragmentation while simultaneously elevating respiration and suppressing apoptosis^{13–17}. HCMV is a scourge to the immunocompromised, representing the leading viral cause of birth defects and transplant rejection. Predicted to be related to the metabolic rewiring induced by this virus infection, HCMV is also recognized as oncomodulatory and a contributor to heart disease^{18–23}.

This unusual structure-function relationship represented by fragmented mitochondria with increased bioenergetics is also seen in other disease states, such as some cancers²⁴ and diabetes^{25–27}. However, it remains largely unclear what is mechanistically different about this form of mitochondria fragmentation compared to a fragmentation that decreases respiration. A potential explanation for this mechanistic discrepancy is that the relative rates of midzone and peripheral fission dictate the bioenergetic state of the fragmented mitochondria population. However, the balance between these forms of fission have not been studied in any disease state.

The function of fragmented mitochondria may also be regulated downstream of the actual fission event through altered membrane contact sites (MCSs), which are increasingly recognized as critical regulators of organelle structure-function²⁸. MCSs are protein-mediated interactions between two or more organelles that are essential for core biological processes, such as metabolite transfer and organelle remodeling²⁹. Despite the ubiquitous nature of these contacts, MCSs remain understudied in many disease contexts, including human viral infections. We recently discovered that HCMV infection modulates MCS proteins across its 120-h replication cycle³⁰. Establishing a previously uncharacterized hallmark of HCMV infection, we showed that endoplasmic reticulum (ER)–mitochondria MCSs are remodeled from the classical tubule crossings^{31,32} to a mitochondria–ER encapsulation structure, which we termed MENC³⁰. Becoming the dominant ER–mitochondria MCS by 72 h post infection (hpi) in HCMV-infected cells, MENCs are formed from stable and asymmetric mitochondria cupping by an ER tubule³⁰. Furthermore, known MCS proteins PTPIP51 and VAP-B^{33–35} were found to re-localize to MENCs by 72 hpi with HCMV³⁰. However, how these uncharacterized structures are formed and what their functions are for either cellular homeostasis or HCMV replication remained unknown. In addition, their assembly and functions in other disease states and connected pathologies have not been investigated.

Here, we address the question of how, in certain biological contexts, mitochondrial fragmentation leads to increased bioenergetics. We report the discovery that mitochondrial progenies derived from peripheral fragmentation can be protected from mitophagy and result in elevated bioenergetic output through a mechanism leveraging ER–mitochondria and inter-mitochondria contacts. Using live-cell super-resolution microscopy, cryo-tomography, proteomics, and metabolic assays, we discover the implementation of this mechanism during HCMV infection. A broader relevance for such a mechanism is

further demonstrated by our finding that ER–mitochondria membrane contacts also increase fragmented mitochondria bioenergetics in metastatic melanoma cells. Our findings offer a previously unrecognized model for how alterations to mitochondria fission/fusion rates and MCS can promote the survival and activity of fragmented mitochondria.

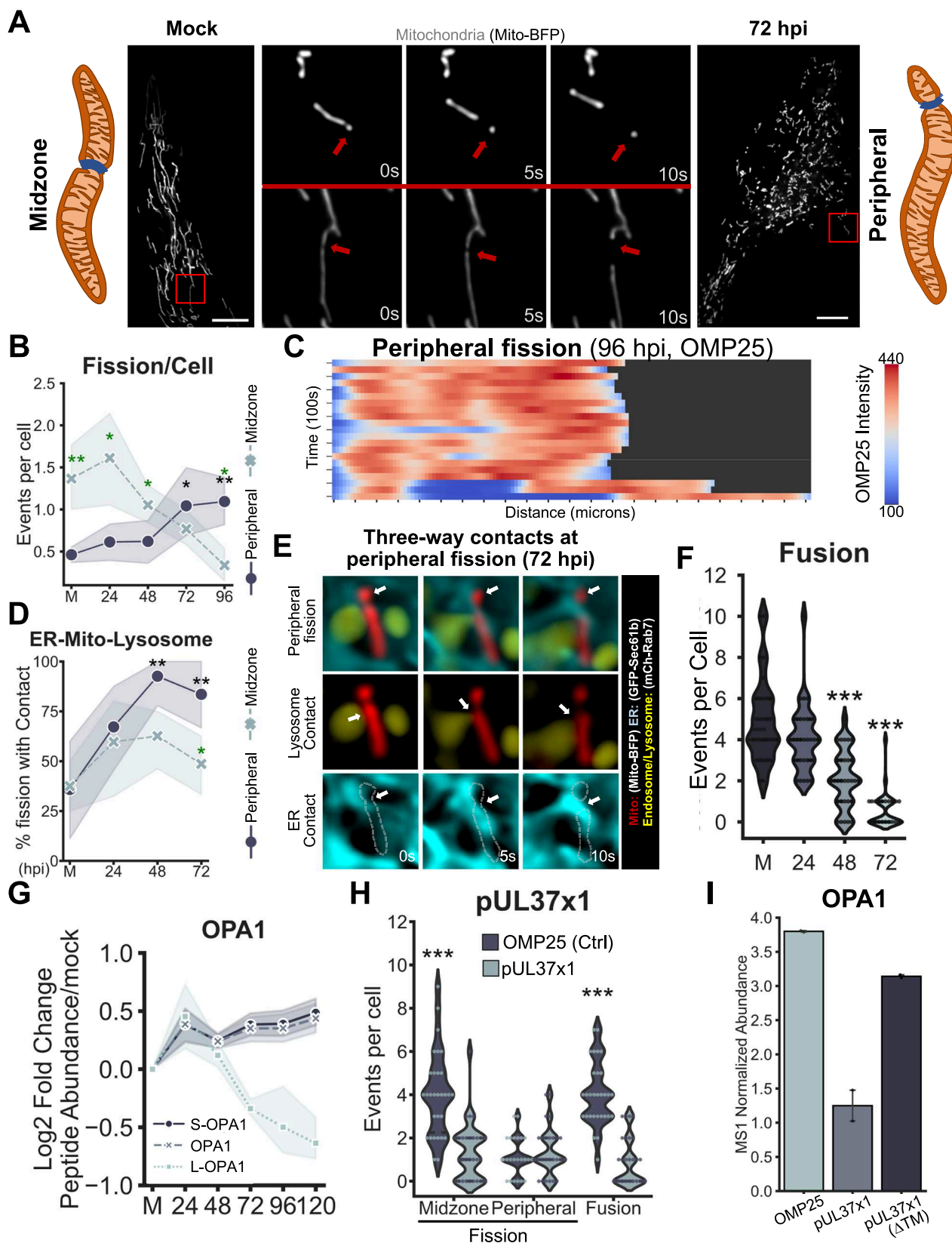
Results

HCMV infection induces mitochondria fragmentation through peripheral fission coupled with fusion suppression

To address how HCMV infection induces mitochondria fragmentation while simultaneously promoting respiration, we used live-cell super-resolution microscopy to assess the type of fission induced³. First, we validated the presence of midzone and peripheral fission in uninfected (mock) and HCMV-infected fibroblasts expressing the mitochondria matrix marker mito-BFP (Fig. 1A, Supplementary Fig. S1A, and Supplementary Movies S1 and 2). However, our quantification of hundreds of fission movies led to several surprising findings. First, we find that HCMV has no significant impact on the total number of mitochondria fission events, contrary to the evident fragmentation (Supplementary Fig. S1B). Second, by quantifying the type of fission occurring, we determine that HCMV infection elevates peripheral fission while decreasing midzone fission (Fig. 1B and Supplementary Fig. S1C). The proportion of peripheral fission events increases from 25% in mock cells to >75% by 96 hpi. This shift is due to both a progressive decrease in midzone fission, starting at 48 hpi, and a two-fold increase in peripheral fission at 72 hpi. To validate that these peripheral fission events were indeed the result of individual mitochondria splitting, we imaged infected cells expressing an outer mitochondria membrane marker (OMP25). As shown in the kymograph for representative mitochondria, a contiguous signal prior to fission was observed (Fig. 1C and Supplementary Fig. S1D). A slight dip in OMP25 signal marks the fission site, likely indicating ER constriction. Peripheral fission was further confirmed using mito-Dendra2 expression³⁶, which allowed us to selectively photoconvert and track individual mitochondria through fission (Supplementary Fig. S1E). These results demonstrate a previously unrecognized ability for a viral infection to modulate the balance between peripheral and midzone mitochondria fission.

Contacts between mitochondria and the ER and lysosomes are known to regulate mitochondria fission and to be differentially regulated during peripheral and midzone fission events³. Hence, we live imaged markers for the ER, lysosome/late endosomes, and mitochondria in mock and infected cells (Fig. 1D, E and Supplementary Fig. S1F, G). Quantification of ER contacts showed their presence at nearly all fission events, regardless of the fission type or infection timepoint (Supplementary Fig. S1F). Conversely, lysosomes displayed different contact frequencies between uninfected and infected cells. In mock cells, lysosomes were present at ~35% of all midzone and peripheral mitochondrial fission events (Fig. 1D and Supplementary Fig. S1G). By 48 hpi, however, more peripheral fission events (~90%) were marked by lysosomes than midzone (~60%).

Given that the total number of fission events remained consistent, we next assessed whether the accumulation of peripherally fragmented mitochondria is also facilitated by the inhibition of fusion. Indeed, we find that, starting at 48 hpi, mitochondria fusion is decreased (Fig. 1F and Supplementary Movie S3). This temporality matches the known increase in mitochondria fragmentation^{14,37}. To determine the molecular cause of this decline in fusion, we assessed the abundance of mitochondria fusion proteins OPA1, mitofusin 1 (MFN1), and mitofusin 2 (MFN2). Consistent with previous results, we find that MFN2 abundance initially increases then steadily declines throughout infection^{16,30} (Supplementary Fig. S2A). Conversely, OPA1 and MFN1 abundances increase with infection (Fig. 1G and Supplementary Fig. S2A). However, this initial analysis of OPA1 abundance does not differentiate between the long and short cleavage states of



OPA1, L-OPA1 and S-OPA1, respectively^{38,39}. While dependent on how the cleavage occurs^{40,41}, S-OPA1 lacks the ability to induce mitochondria fusion, while retaining other functions of L-OPA1 in maintaining cristae architecture, mitochondria bioenergetic output, and cell survival during oxidative stress^{38,41-43}. By analyzing ~50 precursors found throughout the OPA1 protein sequence, we find that

peptides from within the first 180 amino acids, which are only present in L-OPA1, decrease in abundance with infection (Fig. 1G and Supplementary Fig. S2B). The remainder of the protein, which is found in S- and L-OPA1, increases and then plateaus. These findings show that HCMV specifically upregulates S-OPA1, while concurrently decreasing L-OPA1.

Fig. 1 | HCMV infection induces mitochondria fragmentation through peripheral fission coupled with fusion suppression. **A** Representative images of mitochondria labeled with Mito-BFP in uninfected (mock) and HCMV-infected cells at 72 h post infection (hpi). Center ROIs show timelapses of midzone (bottom) and peripheral (top) mitochondria fission. Red arrows indicate the fission site. Scale bar is 10 μ m. **B** Number of peripheral or midzone fission events per cell; cells per replicate ≥ 10 , $n \geq 5$ biological replicates, total of 303 cells and 581 fission events analyzed. Exact *P* values - Midzone: mock vs. 72 hpi = 0.041; Mock vs. 96 hpi = 0.003; Peripheral: Mock vs. 72 hpi = 0.039; mock vs. 96 hpi = 0.015; Mock: Peripheral vs. Midzone = 0.006; 24 hpi: Peripheral vs. Midzone = 0.019; 48 hpi: Peripheral vs. Midzone = 0.049; 96 hpi: Peripheral vs. Midzone = 0.006. **C** Kymograph of peripheral mitochondria fission with each slice (top to bottom) representing a frame. Images from select frames shown in Supplementary Fig. S1D. **D** Quantification of contact frequency for three-way contacts between ER, mitochondria, and lysosomes. Data points indicate total contact events divided by total fissions for peripheral and midzone mitochondria fission per replicate; cells per replicate ≥ 10 , $n \geq 3$ biological replicates, total of 251 fission events across 214 cells. Exact *P* values; 48 hpi: Midzone vs. Peripheral = 0.058; 72 hpi: Midzone vs. Peripheral = 0.017; Peripheral: Mock vs. 48 hpi = 0.025; Peripheral: Mock vs. 72 hpi = 0.025. **E** Representative timelapse of peripheral fission at 72 hpi with mitochondria labeled with Mito-BFP (red), ER with GFP-Sec61 β (cyan), and lysosomes with mCh-Rab7

(yellow). Top white arrows point to the fission site, middle white arrows point to mitochondria-lysosome contact, and the bottom white arrows point to ER-mitochondria contact ($4 \times 4 \mu$ m ROIs). **F** Quantification of total fusion events observed per cell. Ten cells per replicate, $n = 3$ biological replicates, 350 fusion events across 120 cells. Exact *P* values; Mock vs. 24 hpi = 0.067; Mock vs. 48 hpi = 7.34×10^{-8} ; Mock vs. 72 hpi = 2.35×10^{-13} . **G** Comparative quantification of all OPA1 peptides (OPA1), peptides found in S-OPA1 (S-OPA1) or peptides that are only found in L-OPA1 (L-OPA1). Quantification by DIA-MS, $n = 3$. **H** Quantification of mitochondria fusion as well as midzone and peripheral fission following control (OMP25) or UL37x1 expression. $n = 30$ cells, 239 fission events and 148 fusion events analyzed. Exact *P* values; Peripheral: pUL37x1 vs. OMP25 = 0.370; Midzone: pUL37x1 vs. OMP25 = 8.878×10^{-8} ; Fusion: pUL37x1 vs. OMP25 = 4.429×10^{-13} ; Total fission events: pUL37x1 vs. OMP25 = 3.34×10^{-5} . **I** Quantification of OPA1 abundance following either control or expression of full-length pUL37x1, or a mutant lacking the transmembrane domain (UL37x1 dTM). Quantification by DIA-MS, $n = 2$ replicates. hpi hours post infection, mito mitochondria, ER endoplasmic reticulum, mCh mCherry, s seconds, M mock. Data are presented as mean values with 95% confidence intervals. Black asterisks indicate statistical comparison to uninfected cells, while green asterisks indicate comparison between conditions at the same time-point. **P* ≤ 0.05 , ***P* ≤ 0.01 , and ****P* ≤ 0.001 using a Welch's *t* test. Source data are provided as a Source Data file.

To understand how HCMV is inducing this fusion/fission imbalance, we investigated the roles of the two main viral proteins known to target mitochondria—pUL37x1 and pUL13. pUL37x1, or vMIA, is a critical regulator of mitochondria dynamics during HCMV infection, being an inhibitor of apoptosis, needed for calcium release from the ER, and necessary and sufficient for mitochondria fragmentation^{13,14,17,44–47}. The means through which pUL37x1 induces mitochondrial fragmentation remained unclear. In agreement with previous reports, we find the expression of pUL37x1 outside the context of infection to be sufficient for inducing mitochondria fragmentation (Supplementary Fig. S2C). Through quantification of mitochondria fission and fusion, we demonstrate that pUL37x1 expression decreases midzone fission and mitochondria fusion (Fig. 1H and Supplementary Fig. S2D). pUL37x1 expression is also sufficient to decrease OPA1 abundance, while causing a slight, but not significant, decrease in MFN2 abundance (Fig. 1I and Supplementary Fig. S2E). These effects were partially rescued when the pUL37x1 transmembrane domain was deleted (Fig. 1I and Supplementary Fig. S2E), demonstrating the importance of pUL37x1 mitochondria localization that is conferred by this functional domain⁴⁴. The viral protein pUL13 is also known to regulate mitochondria structure-function, altering the mitochondria ultrastructure and being necessary and sufficient for elevating mitochondria respiration¹⁵. Upon infection with a UL13 deletion HCMV strain (Δ UL13)¹⁵, we find that mitochondria fragmentation is comparable to WT HCMV-infected cells (Supplementary Fig. S2C). Peripheral fission events are still evident upon Δ UL13 infection, indicating that UL13 does not contribute to this fission/fusion dysregulation and suggesting that pUL13 functions downstream of pUL37x1 (Supplementary Fig. S2F). These data establish that peripheral fission and suppression of mitochondria fusion are at the heart of pUL37x1-dependent mitochondria fragmentation during HCMV infection.

Mitophagy is suppressed during HCMV infection

As peripheral fission has been linked to mitochondria degradation³, we next tested whether the observed increase in peripheral fission during HCMV infection induced a concurrent upregulation of mitophagy. The role of general autophagy in HCMV infection is unclear. LC3-II and other autophagy-related proteins were reported to be upregulated during HCMV infection and necessary for efficient viral replication^{48,49}. Contrasting reports suggested that autophagy is antiviral, suppressing HCMV replication^{50–53}. Furthermore, the modulation of mitochondrial

autophagy (i.e., mitophagy) during HCMV infection has not been previously assessed. To quantify mitophagy, we first used immunofluorescence microscopy to image endogenous LC3 at mitochondria (Fig. 2A). The total abundance of LC3 puncta initially dipped at 24 hpi, then increased through 48 and 72 hpi (Supplementary Fig. S3A). As mitochondria also proliferate during HCMV infection, it is not surprising that we observe a higher percentage of the LC3 population to be in contact with mitochondria as infection progresses (Fig. 2B). However, the fluorescence intensity of these puncta, which is a proxy for LC3 concentration, follows the opposite trend, increasing at 24 hpi then decreasing by 72 hpi (Supplementary Fig. S3B). The fluorescence intensity of LC3 puncta not contacting mitochondria was consistently higher than those puncta in contact with mitochondria across infection (Fig. 2B). Moreover, the size of LC3 puncta in contact with mitochondria during infection appears to be much smaller than what would be expected for an autophagosome⁵⁴. Altogether, these observations suggest that mitophagy is not significantly activated during HCMV infection.

To confirm that the LC3 puncta observed at mitochondria do not induce mitophagy, we expressed the mitochondria-localized ratio-metric fluorophore and pH sensor mtKeima⁵⁵. This approach uses the ratio of the 565 nm/405 nm laser excitations to identify mitochondria undergoing mitophagy. To analyze these data, we developed a computational pipeline that segments mitochondria and quantifies mtKeima intensity in a non-biased manner. We validated this workflow by treating mock cells expressing mtKeima with the mitophagy-inducing protonophore CCCP with or without the autophagy inhibitor Bafilomycin A (BFA) and compared mtKeima signal to our control DMSO treatment (Supplementary Fig. S3C, D). As an additional validation, we expressed a Rab7^{Q67L} mutant that colocalizes with parkin at mitophagosomes⁵⁶. Increased mtKeima fluorescence was evident at mitochondria encapsulated by Rab7^{Q67L}-marked vesicles (Supplementary Fig. S2E). By applying this workflow across HCMV infection, we observed suppression of mitophagy (Fig. 2C, D and Supplementary Fig. S3F, G). This agrees with our LC3 staining results, given that we did not observe a large accumulation of LC3 at mitochondria, as it would have been expected for mitophagosome formation^{15–17}.

To assess how mitophagy suppression is controlled at the protein level, we quantified mitophagy regulatory proteins across HCMV replication (Fig. 2E). While we were unable to detect the major known drivers of mitophagy Parkin and PINK1, we found that HCMV infection

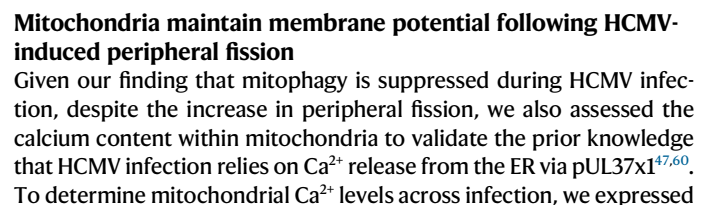


Fig. 2 | HCMV-induced peripheral fission paradoxically produces functional progenies. **A** Representative microscopy images of LC3 localization. Scale bar is 1 μ m. **B** Left: Percent LC3 puncta in contact with mitochondria. Right: Quantification of endogenous LC3 abundance (immunofluorescence intensity) either in isolated LC3 puncta or in LC3 puncta in contact with mitochondria; Mock = 66, 24 hpi = 68, 48 hpi = 65, 72 hpi = 72 total cells analyzed for each timepoint, $n = 3$ biological replicates, total of 267 cells. **C** Representative images of mitochondria expressing mtKeima excited by either 405 nm or 565 nm laser. **D** Quantification of mitochondria undergoing mitophagy as indicated by the median 565 nm to 405 nm excitation ratio of mtKeima for each segmented mitochondria. Infected and untreated mock cells consist of ≥ 13 cells per replicate, $n = 3$ biological replicates. Right: scheme showing that mitochondria pH shifts from ~ 8 to ~ 5.5 during mitophagy, which alters mtKeima fluorescence. **E** Log2 fold-change protein abundance compared to mock for mitophagy-related proteins. DIA acquisition, $n = 3$ replicates. **F** Representative image of mitochondrial potential given by the intensity of TMRE and outer mitochondria membrane labeled with OMP25 during a peripheral fission event at 72 hpi. White arrows point to fission site (scale bar = 3 μ m). **G** Quantification of mitochondria potential change following either peripheral or midzone mitochondria fission across HCMV infection time. Top: Mitochondria membrane

potential quantified following treatment with 200 nM TMRE. Membrane potential was quantified as Log2 of the max TMRE intensity of the progeny near the fission site divided by the max TMRE intensity of the parent mitochondria at the fission site; Mock = 72, 24 hpi = 64, 48 hpi = 72, 72 hpi = 72 total cells analyzed for each timepoint; $n = 3$ biological replicates. Bottom: Mitochondria membrane potential quantified following treatment with 25 nM TMRE. Membrane potential quantified as the Log2 of the mean TMRE intensity of the progeny divided by the mean of the parent; Mock = 76, 48 hpi = 48 total cell imaged for each timepoint, $n = 3$ biological replicates. Boxplot shows the median as well as upper and lower quartiles of the data with the whiskers showing the full distribution, excluding outliers. **H** Cartoon representing our findings of mitochondria undergoing peripheral fission at three-way ER-mito-lysosome contacts, the progenies of which exhibit suppressed mitophagy as well as elevated membrane potential relative to mock. $\Delta\Psi_m$ = mitochondria membrane potential. $\Delta\Psi_m$, mitochondria membrane potential, hpi hours post infection, mito mitochondria, s seconds, M mock. Data are presented as mean values with 95% confidence intervals. Black asterisks indicate statistical comparison to uninfected cells, while green asterisks indicate comparison between conditions at the same timepoint. * $P \leq 0.05$, ** $P \leq 0.01$, and *** $P \leq 0.001$ using a Welch's t test. Source data are provided as a Source Data file.

the plasmid mtCameleon, which localizes to mitochondria and increases in fluorescence when bound to Ca^{2+} (see refs. 61,62). The cameleon sensor was co-expressed along with mito-pHRed, a mitochondria-localized pH sensor⁶³, to account for alterations in mitochondria pH that can impact mtCameleon fluorescence⁶⁴. As expected, we observed an increase in mitochondria calcium with infection (Supplementary Fig. S3H).

We next asked if mitochondria also maintain their membrane potential ($\Delta\Psi_m$) following peripheral or midzone fission. The $\Delta\Psi_m$ is a function of mitochondria respiration and thus an indicator of mitochondria bioactivity⁶⁵. We quantified $\Delta\Psi_m$ by staining with the potentially sensitive dye TMRE⁶⁶, which we validated to respond to CCCP treatment in a dose-dependent manner (Supplementary Fig. S4A). To determine how peripheral and midzone fission may be influencing $\Delta\Psi_m$, we compared the TMRE intensity of the parent mitochondria just prior to fission to the TMRE intensity of the progeny mitochondria just following fission. As expected, in mock cells midzone fission had little impact on the $\Delta\Psi_m$, while peripheral fission decreased it (Fig. 2F, G and Supplementary Fig. S4B). However, as the infection progressed, the $\Delta\Psi_m$ was no longer reduced following peripheral fission, with almost no impact seen by 48 hpi. We validated these results using two different concentrations of TMRE (200 and 25 nM), as well as two different methods of quantification. Thus, we show that the progenies from HCMV-induced peripheral mitochondria fission are not specifically degraded and instead exhibit rescued membrane potential and calcium import (Fig. 2H). These functions increase mitochondria respiratory capacity, thus allowing mitochondria to meet the high-energy demands of HCMV infection, in particular during virus assembly occurring at 72 hpi⁶⁷.

Peripheral fission and mitochondria fusion suppression lead to mitochondria-ER encapsulations (MENCs)

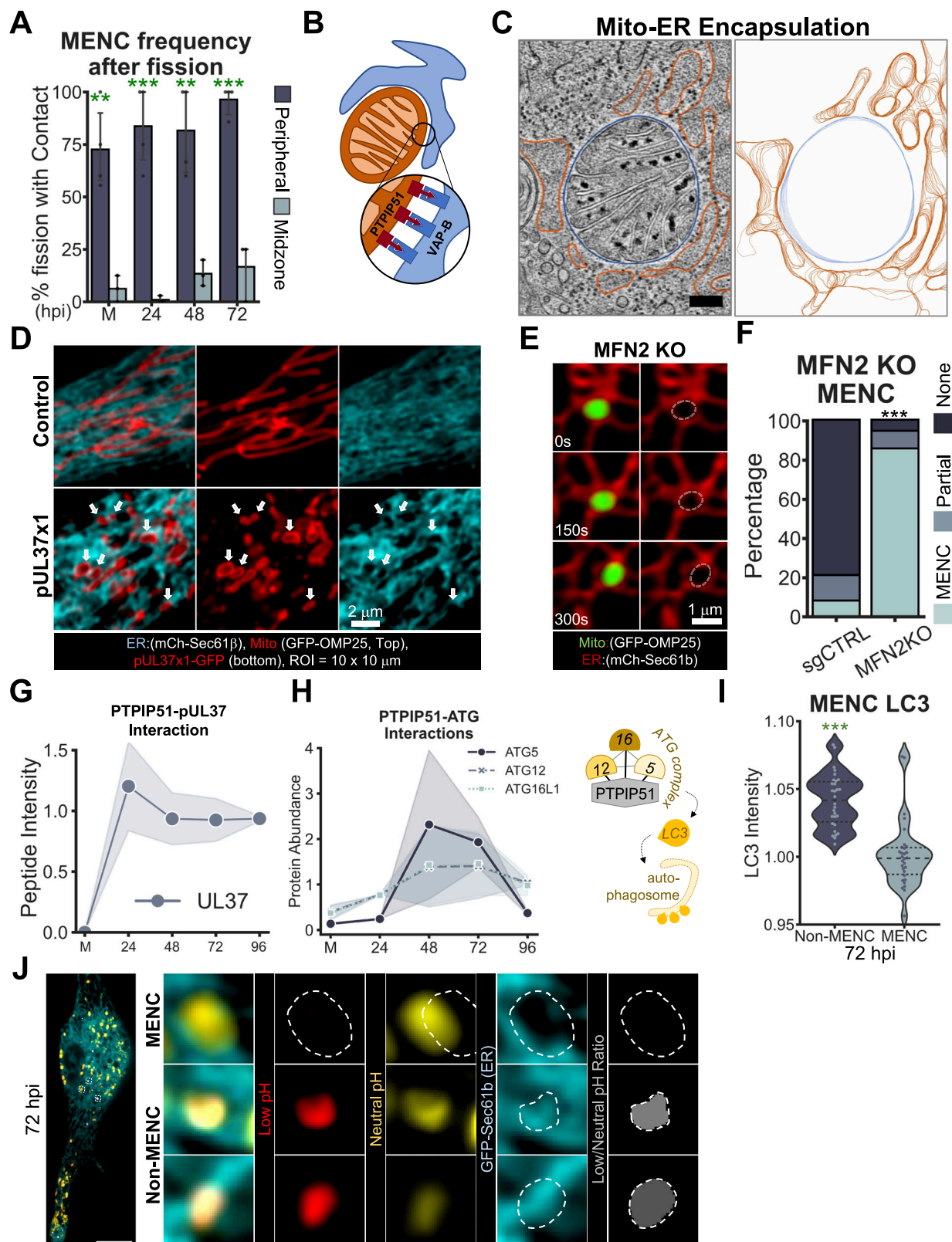
Having discovered the paradox that infection-induced peripheral fission progenies maintain their membrane potential, we asked what the molecular basis of this phenotype is. We found that, unlike midzone fission, most peripheral fission events lead to the formation of mitochondria-ER encapsulations (MENCs) (Fig. 3A). MENCs are an MCS structure we recently characterized, whereby ER tubules form a stable and asymmetric cup around mitochondria³⁰ (Fig. 3B). To validate the formation of these structures, we used electron cryo-tomography (cryo-ET). At 72 hpi, when the predominant ER-mitochondria contact sites are MENCs³⁰, tomograms of HCMV-infected cells showed asymmetric ER encapsulations of mitochondria (Fig. 3C and Supplementary Movie S4). This asymmetric encapsulation is the hallmark of a MENC, and the ER (orange) was within 15 nm of the mitochondria (blue), in line with this structure representing a true MCS²⁸.

Given our finding that expressing the viral factor pUL37x1 toggles the mitochondrial fission/fusion balance (Fig. 1H, I), we next tested if pUL37x1-induced fragmentation is also sufficient to drive MENC formation. Indeed, we observe abundant MENCs upon pUL37x1 expression (Fig. 3D). Further indicating that pUL13 acts downstream of fission and MENC formation, we also found that pUL13 is dispensable for MENC formation (Supplementary Fig. S4C). However, pUL37x1 is known to have several functions unrelated to mitochondria fragmentation^{45,68-70}. Therefore, to determine if pUL37x1-dependent mitochondria fusion suppression is what drives MENC formation, we also assessed MENC prevalence following knockout (KO) of the host fusion protein MFN2⁷¹ (Supplementary Fig. S4D). We find that following MFN2 KO, >80% of the mitochondria analyzed were in MENCs (Fig. 3E, F). This MENC percentage is on par with levels at late stages of HCMV infection, when MENCs are most upregulated³⁰. Therefore, we establish that in mock and infected cells, MENCs are preferentially formed following peripheral fission, and that the prevalence of MENCs can be modulated by suppressing mitochondria fusion.

Mitochondria are protected from mitophagy at MENCs

Despite the abundance of MENCs during infection, and the established importance of MENC-resident protein PTPIP51 for HCMV replication³⁰, the function of MENCs remains unknown. PTPIP51 has several core functions at ER-mitochondria contacts that could benefit viral replication, including the regulation of calcium homeostasis, autophagy, and phospholipid transfer^{33-35,72,73}. To determine which of these may be at play during HCMV infection, we isolated endogenous PTPIP51 in mock and HCMV-infected cells using immunoaffinity purification and analyzed its interactions by mass spectrometry (IP-MS) (Supplementary Fig. S5A and Supplementary Data 1). To gain further resolution on potential PTPIP51 interactions, particularly those that may be low abundance, we also used targeted MS (parallel reaction monitoring or PRM) to monitor several host and viral proteins.

Given that PTPIP51 becomes more enriched at MENCs as infection progresses³⁰, proteins that show increased interaction abundance with PTPIP51 across infection are also likely to be MENC-localized. We therefore performed k-means clustering on the identified PTPIP51 interactions and GO-term enrichment on the proteins whose interaction abundance with PTPIP51 increased from mock to 72 hpi (Supplementary Fig. S5C-E). Through these analyses, we found that PTPIP51 associates with proteins involved in post-translational modifications, autophagy, and mitochondria organization (respiratory chain assembly) (Supplementary Fig. S5D). As expected for an MCS protein that is present at the interface of several different organelles, we observed that PTPIP51 interacted with proteins from several different



compartment, likely representing both direct and indirect interactions. Consistent with our previous IP-MS study of pUL37x1 interactions⁷⁰, both PRM and untargeted MS assays pointed to an interaction between PTIP51 and pUL37x1 starting early in infection (Fig. 3G and Supplementary Fig. S6A).

In addition to pUL37x1, PTIP51 interacted with HCMV-encoded proteins across temporal gene classes (Supplementary Fig. S6A).

Among these was TRS1, a known negative regulator of autophagy during HCMV infection⁵³. PTIP51 also interacted with several host autophagy proteins (Supplementary Fig. S5D, E). Among these were all three components of the autophagy elongation complex ATG5/12/16L (Fig. 3H). This complex acts as an E3 conjugating enzyme and is necessary for LC3 lipidation and thus autophagosome maturation^{74,75}. Hence, these observations led us to ask whether MENCs and their

Fig. 3 | Mitochondria–ER encapsulations (MENC) follow peripheral fission and promote bioenergetics. **A** Quantification of peripheral or midzone fission events leading to MENC formation. Each data point represents a biological replicate; Mock = 67, 24 hpi = 67, 48 hpi = 73, 72 hpi = 71 total cells analyzed for each timepoint; Midzone = 3, peripheral = 4 biological replicates. **B** Cartoon representation of a MENC. Cutout shows PTPIP51 and VAP-B localization to the mitochondria and ER interfaces of MENCs, respectively. **C** Left: Slice through a tomogram and right: 3D segmentation of an HCMV-infected cell at 72 hpi showing Mito-ER encapsulation (whole volume shown in Supplementary Movie S4). The mitochondrial and ER membranes are outlined in blue and brown, respectively. Scale bar is 200 nm. Representative of one biological replicate with 23 cells across two grids being selected for FIB-milling. Out of these, 6 lamella sites were successfully polished and used for cryo-ET data acquisition. In total 34 tilt series were acquired of which 27 contained mitochondria and ER in close proximity. **D** Live-cell microscopy of pUL37x1-induced MENC formation. White arrows point to MENCs. (ROI = $10 \times 10 \mu\text{m}$). **E** Representative images of MFN2 KO-induced MENC formation. Timelapse shown top to bottom. (ROI = $3 \times 3 \mu\text{m}$). **F** Quantification of MFN2 KO-induced MENC formation. Ten mitochondria per cell, 10 cells per condition, $n = 3$ biological

replicates; total of 600 mitochondria. **G** PTPIP51 interaction with pUL37x1 as quantified by targeted MS (PRM). **H** Left: PTPIP51-ATG interaction abundance as quantified by DDA-MS. (2 biological replicates, except for 24 hpi). Right: Cartoon representation indicating the function of PTPIP51 interactors the ATG5/12/16L complex in autophagosome maturation. **I** Quantification of LC3 intensity in MENC and non-MENC mitochondria at 72 hpi. Shown as LC3 intensity per cell. 10 MENC and non-MENC mitochondria quantified per cell; 10 cells per replicate; $n \geq 3$ biological replicates, 600 mitochondria across 30 cells. **J** Representative microscopy showing colocalization of acidified mitochondria (as shown through mtKeima ratiometric imaging) with the ER as well as the lack of acidification in MENC mitochondria. Scale bar = $10 \mu\text{m}$. hpi hours post infection, mito mitochondria, ER endoplasmic reticulum, mCh mCherry, s seconds, M mock, MENC mitochondria–ER encapsulation, KO knockout. Data are presented as mean values with 95% confidence intervals. Black asterisks indicate statistical comparison to uninfected cells, while green asterisks indicate comparison between conditions at the same timepoint. * $P \leq 0.05$, ** $P \leq 0.01$, and *** $P \leq 0.001$ using a Welch's t test. Source data are provided as a Source Data file.

resident protein PTPIP51 function to regulate mitophagy during infection. To address this, we sought to first validate the PTPIP51-ATG interaction. We performed reciprocal IP-PRM on endogenous ATG12 in mock and 72 hpi cells. We found that, indeed, ATG12 interacts with PTPIP51 (Supplementary Fig. S6B). In addition, unlike PTPIP51, we noted that ATG12 loses its interaction with other outer mitochondria membrane proteins (VDAC1-3) during infection. This suggests that the ATG12-PTPIP51 interaction is not only driven by their localization to mitochondria, as otherwise we would have also expected to see sustained ATG12-VDAC interactions. Furthermore, we find that ATG12 displays increased interactions with ATG5, ATG16L, and ATG7 at 72 hpi. Conversely, while ATG12 interacts with LC3s (LC3A/B and GBRAP) in mock, these interactions are stunted during infection. These findings led us to speculate that the ATG5/12/16L complex is not activating LC3 during infection, which may result in suppressed mitophagy at MENCs.

To test if mitophagy is dysregulated at MENCs during HCMV infection, we first quantified endogenous LC3 intensity co-localizing at MENC and non-MENC mitochondria during infection. We found that MENCs had decreased LC3 intensity (Fig. 3I). We next expressed mtKeima along with an ER marker to visualize mitophagy at MENCs (Fig. 3J). This analysis demonstrated that mitochondria undergoing mitophagy were not in MENCs. Furthermore, MENC mitochondria did not show any signs of acidification.

To determine if PTPIP51 contributes to the decrease in mitophagy at MENCs, we performed siRNA-mediated knockdown (KD) of PTPIP51 followed by quantification of mitophagy-associated proteins. We validated the efficacy of our KD using MS as well as a TUNEL assay and qPCR to quantify cell death and ISG expression (Supplementary Fig. S6C–E). In uninfected cells, we saw no difference in cell death or ISG expression, with a slight increase in both effects during infection. Building on our findings that HCMV infection downregulates mitophagy proteins (Fig. 2E), we find that PTPIP51 KD suppresses the downregulation of several autophagy/mitophagy-related proteins (Supplementary Fig. S6C). These include proteins involved in the initialization of autophagosome/mitophagosome formation, as well as throughout the maturation cycle of these structures. Notably, PTPIP51 KD resulted in an increase in the abundances of both LC3 and GABARAPL2.

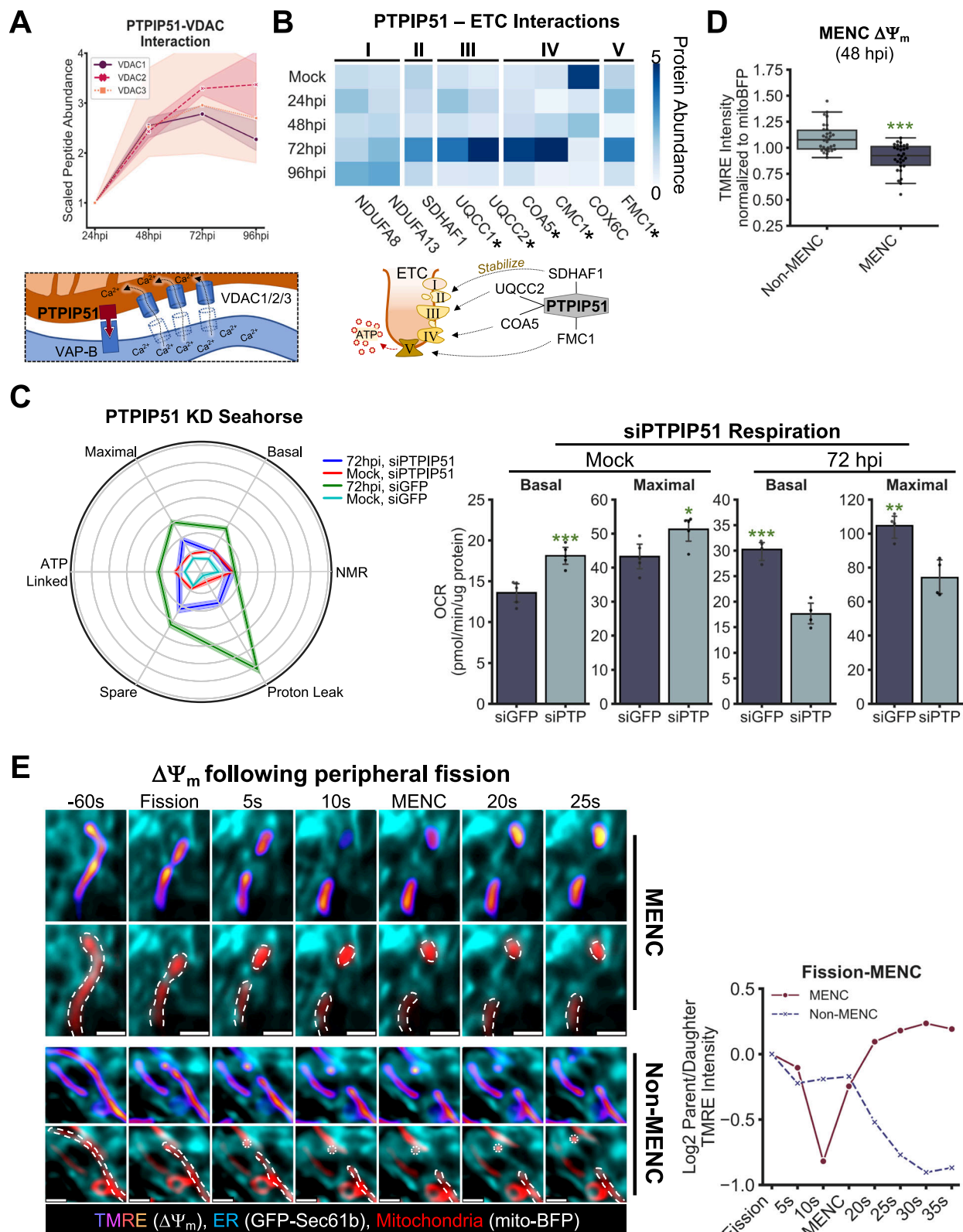
Altogether, our findings establish that peripheral fission and suppression of fusion lead to MENC formation, where mitochondria are protected from mitophagy during infection.

MENC-associated PTPIP51 is necessary for elevated respiration during infection

Our temporal protein interaction study indicated that PTPIP51 is primed to regulate metabolism through multiple pathways (Supplementary Fig. S5C–E), suggesting that MENCs may also be important

for regulating mitochondria bioenergetics. First, we find that PTPIP51 interacts with the IP₃R and VDAC cation channels (Fig. 4A and Supplementary Fig. S6F). VDACS are localized to the outer mitochondria membrane and cooperate with IP₃R on the ER to regulate mitochondria calcium import, and by extension the turning of the TCA cycle⁷⁶. These interactions agree with the known function of PTPIP51 at ER-mitochondria contacts in regulating calcium import into the mitochondria^{33,35}. Further downstream of the TCA cycle, we find that PTPIP51 interacts with several components of the electron transport chain (ETC), as well as proteins that promote the assembly and stabilization of ETC complex II, III, IV, and V⁷⁷ (Fig. 4B). All of the identified ETC interactors are nuclear-encoded, thus indicating how PTPIP51, which sits on the outer mitochondria membrane, could be interacting with ETC-related proteins, which localize to the inner mitochondria membrane. Finally, we also find that PTPIP51 interacts with several components of the MICOS (mitochondria contact and cristae organization system) and MIB (mitochondria intermembrane space bridging complex) (Supplementary Fig. S6G). These complexes are critical for mitochondria ultrastructure and represent a regulatory and physical linkage between the outer and inner mitochondria membranes^{78,79}.

The abundance of nearly all these interactions with metabolism-associated proteins increased through 72 hpi. This prompted us to propose that PTPIP51 at MENCs may regulate the assembly of the ETC, possibly contributing to the known increase in respiration following HCMV infection^{15–17}. Using a live-cell Seahorse assay, which measures oxygen consumption to quantify respiratory parameters, we find that PTPIP51 siRNA-mediated knockdown (KD) dampens nearly all aspects of respiration at 72 hpi (Fig. 4C and Supplementary Fig. S6H). With the exception of non-mitochondrial respiration, reductions were observed in basal respiration, maximal respiration, ATP-linked respiration, and proton leak upon PTPIP51 KD compared to control during infection. While this assay is not specific to MENCs, as it measures all mitochondria, it is worth considering that we previously established that by 72 hpi the majority of mitochondria are within MENCs³⁰. Furthermore, we find that the role of PTPIP51 in elevating respiration is specific to infection (Fig. 4C), which is when PTPIP51 is enriched at MENCs and is consistent with its interactions with ETC-related proteins during infection. In agreement with the notion that PTPIP51 increases mitochondria respiration at MENCs during infection, we also find that MENC mitochondria exhibit lower membrane potential than non-MENC mitochondria during infection (Fig. 4D). This is due to the phenomenon that membrane potential is dissipated as respiration increases and protons are instead used for ATP phosphorylation. Importantly, while MENC mitochondria displayed lower membrane potential, they were still sufficiently polarized to indicate that they were not dysfunctional.



Altogether, our findings show that peripheral fission and suppression of mitochondria fusion lead to MENC formation, and that MENC-localized PTPIP51 plays a role in elevating mitochondria bioenergetics. To further visualize this mechanism, we used live-cell TMRE analysis. By comparing the TMRE intensity of two peripheral fission events, one that leads to a MENC and one that does not, we observed that only the MENC-associated mitochondria had its

polarization restored after fission (Fig. 4E and Supplementary Movie S5).

MENCs and suppression of mitochondria fusion stabilize inter-mitochondria contacts

In uninfected cells, we observe that contact between two mitochondria commonly leads to mitochondria fusion (Fig. 5A). However, we find

Fig. 4 | PTPIP51 regulates metabolic processes during HCMV infection. **A** Top: Abundance of PTPIP51-VDAC interaction quantified by targeted MS (≥ 2 peptides per protein). Bottom: Cartoon representation of the role of VDAC1/2/3 proteins in calcium import in the mitochondria (brown/orange) from the ER (blue). **B** Top: Abundance of PTPIP51 interaction with the electron transport chain complex (ETC) subunits and ETC assembling proteins (*) (2 biological replicates, except for 24 hpi). Bottom: Cartoon representation of the ETC complex that PTPIP51 interacting proteins stabilize. **C** Quantification of respiratory parameters in mock or 72 hpi HCMV-infected cells following siRNA control (siCTRL) or PTPIP51 KD (siPTPIP51). Left: Radar plot displaying all of the scaled respiratory parameters measured by the Seahorse assay. Right: Bar plots of basal and maximal respiration in these conditions (siGFP = 5, siPTPIP51 = 4 biological replicates). Exact *p* values; Basal: siGFP vs. siPTP = 3.12×10^{-4} ; Maximal: siGFP vs. siPTP = 0.005. **D** Quantification of membrane potential ($\Delta\Psi_m$) of MENC and non-MENC mitochondria. TMRE intensity is normalized to the mito-BFP signal and then scaled to the average membrane potential for each cell. Each data point represents a single cell; 10 cells per replicate; *n* = 3

biological replicates, 90 mitochondria across 30 cells. Boxplot shows the median as well as upper and lower quartiles of the data with the whiskers showing the full distribution, excluding outliers. Exact *P* values; TMRE Intensity: MENC vs. Non-MENC = 8.32×10^{-7} . $\Delta\Psi_m$ mitochondria membrane potential. **E** Left: Representative microscopy images showing mitochondria undergoing peripheral fission, leading to MENC (top) or non-MENC (bottom). Scale bar = 3 μ m. Right: Median TMRE intensity in the progeny is quantified every frame (5 s) for 35 s after fission and plotted as log2 fold change to TMRE intensity during fission, when time = 0. TMRE intensity was first normalized to mito-BFP. $\Delta\Psi_m$ mitochondria membrane potential, hpi hours post infection, mito mitochondria, ER endoplasmic reticulum, s seconds, M mock, MENC mitochondria-ER encapsulation, KD knockdown, ETC electron transport chain, Ca^{2+} calcium, OCR oxygen consumption rate. Data are presented as mean values with 95% confidence intervals. Black asterisks indicate statistical comparison to uninfected cells, while green asterisks indicate comparison between conditions at the same timepoint. **P* \leq 0.05, ***P* \leq 0.01, and ****P* \leq 0.001 using a Welch's *t* test. Source data are provided as a Source Data file.

that during infection mitochondria collisions form temporally stable inter-mitochondria contacts (IMCs) (Fig. 5A). IMCs are junctions between mitochondria that specifically do not lead to full fusion and matrix mixing, but instead coordinate mitochondria bioenergetics through exchange of electrochemical signals or small molecules^{80,81}. These MCSs have been implicated in mitochondria diseases such as Charcot-Marie-Tooth type 2 and cardiovascular disease^{82,83}. We find that IMC stability continually increased across HCMV infection, with the largest increase evident by 72 hpi (Fig. 5B). At 72 hpi, the majority of IMCs were stable for over 3 min, whereas in mock cells, most IMCs lasted less than a minute.

Given that we also observed IMCs upon pUL37x1 expression (Fig. 3D), we next aimed to determine if these interactions are a consequence of suppressed mitochondria fusion. We find that suppression of fusion through MFN2 KO is sufficient to increase IMC temporal stability (Fig. 5C and Supplementary Fig. S7A). As MENCs and IMCs are concurrently prevalent at 72 hpi, we next assessed whether MENCs are associated with increased IMC stabilization. We analyzed our live-cell videos, scoring each IMC as arising from 0, 1, or 2 MENCs (Fig. 5D, E and Supplementary Movie S6). We found that less stable IMCs had a random assortment of MENC and non-MENC mitochondria, while >90% of the more stable IMCs were associated with 2 MENCs. Therefore, while not all MENCs promote IMCs, nearly all stable IMCs were found to arise from MENCs.

To visualize these structures with higher resolution and validate that the observed IMCs represent bona fide MCSs, we used cryo-ET. While we cannot establish stability over time for the IMCs by cryo-ET, we observe mitochondria in close apposition (~10 nm) (Fig. 5F and Supplementary Movie S7), consistent with our live-cell analyses. To assess how these mitochondria could be engaging in IMCs and MENCs simultaneously, we used super-resolution light microscopy to take Z-slices and create a 3D reconstructions of MENC-IMCs taken at 72 hpi (Fig. 5H). We find that ER tubules weave around the site of inter-mitochondria contact. By staining for endogenous PTPIP51, we further find that PTPIP51 is enriched at ER tubules wrapping under or around the site of IMC (Fig. 5G).

IMCs are proviral structures that promote mitochondria respiration

As our results uncovered the formation of stable IMCs upon infection, we asked whether these structures function for the benefit of the virus or the host. To assess this, we used the tethering system developed by Picard et al.⁸⁰, in which FRB and FKBP linker domains are localized to mitochondria and induced to interact upon rapamycin treatment, thereby making stable IMCs. Therefore, this system will promote the formation of IMCs independent of whether they are within MENCs or not. To validate this system for our cell model, we transfected cells with either FRB and FKBP (tether) or FRB and an

outer mitochondria membrane-localized GFP (control). We then treated each of these conditions with either rapamycin or DMSO. While tether expression in the absence of rapamycin caused a slight increase in mitochondria clustering, significantly more tethering was induced upon rapamycin treatment (Supplementary Fig. S7B). We therefore proceeded to infect each of these four conditions and treat with rapamycin at 72 hpi to induce tethering (Supplementary Fig. S7C). We found that IMC induction at 72 hpi caused an over three-fold increase in viral replication compared to all three controls, showing that these structures are proviral (Fig. 6A). To test whether increasing the prevalence of IMC formation can also elevate respiration, we used a Seahorse assay to quantify respiration upon IMC induction. Indeed, at 72 hpi, the activated tether increased ATP-linked, basal, and maximal respiration, as well as spare capacity (Fig. 6E and Supplementary Fig. S8A). Furthermore, this was specific to infection, as tether activation in mock cells had no impact on respiration (Supplementary Fig. S8B).

To further delve into the bioenergetic properties of IMCs during HCMV infection, we turned to TMRE staining and live-cell imaging. We observed that mitochondria appeared to spontaneously depolarize and repolarize, appearing as blinking in live-cell microscopy (Fig. 6B and Supplementary Movie S8). The frequency of these events could be increased by slightly elevating cellular stress via increased laser power. Leveraging this approach allowed us to determine that IMC mitochondria were blinking more frequently and had higher amplitude changes when compared to non-IMC mitochondria from the same cell (Supplementary Fig. S9A, B). In addition, when we averaged all of the TMRE changes over time, we found that IMC mitochondria are cumulatively increasing their TMRE intensity, while non-IMC mitochondria were overall not changing (Supplementary Fig. S9). These findings led us to speculate that during HCMV infection IMCs may coordinate the membrane potentials of the connected mitochondria to help maintain bioactivity. To test this, we quantified the membrane potential flux of the contacting mitochondria when its partner rapidly depolarizes, which we define as decreasing its membrane potential by 40% or more within 3–6 s (1–2 frames). We find that nearly every time a contacting mitochondria was depolarized, its partner displayed increased membrane potential (Fig. 6C and Supplementary Fig. S9C). To confirm that this is not caused by a global change in potential or fluorescence unrelated to mitochondria contact, we also show that a non-contacting mitochondria within the same cell was not bioenergetically coordinated with the depolarizations described above (Fig. 6C). To confirm that this coordination is not occurring by chance, we also showed that a scramble of the contacting mitochondria's TMRE intensity, repeated 1000 \times , showed significantly less coordination than the true IMC results (Fig. 6C). In addition, we find that IMC mitochondria are capable of repolarizing after minutes of depolarization (Supplementary Fig. S9D).

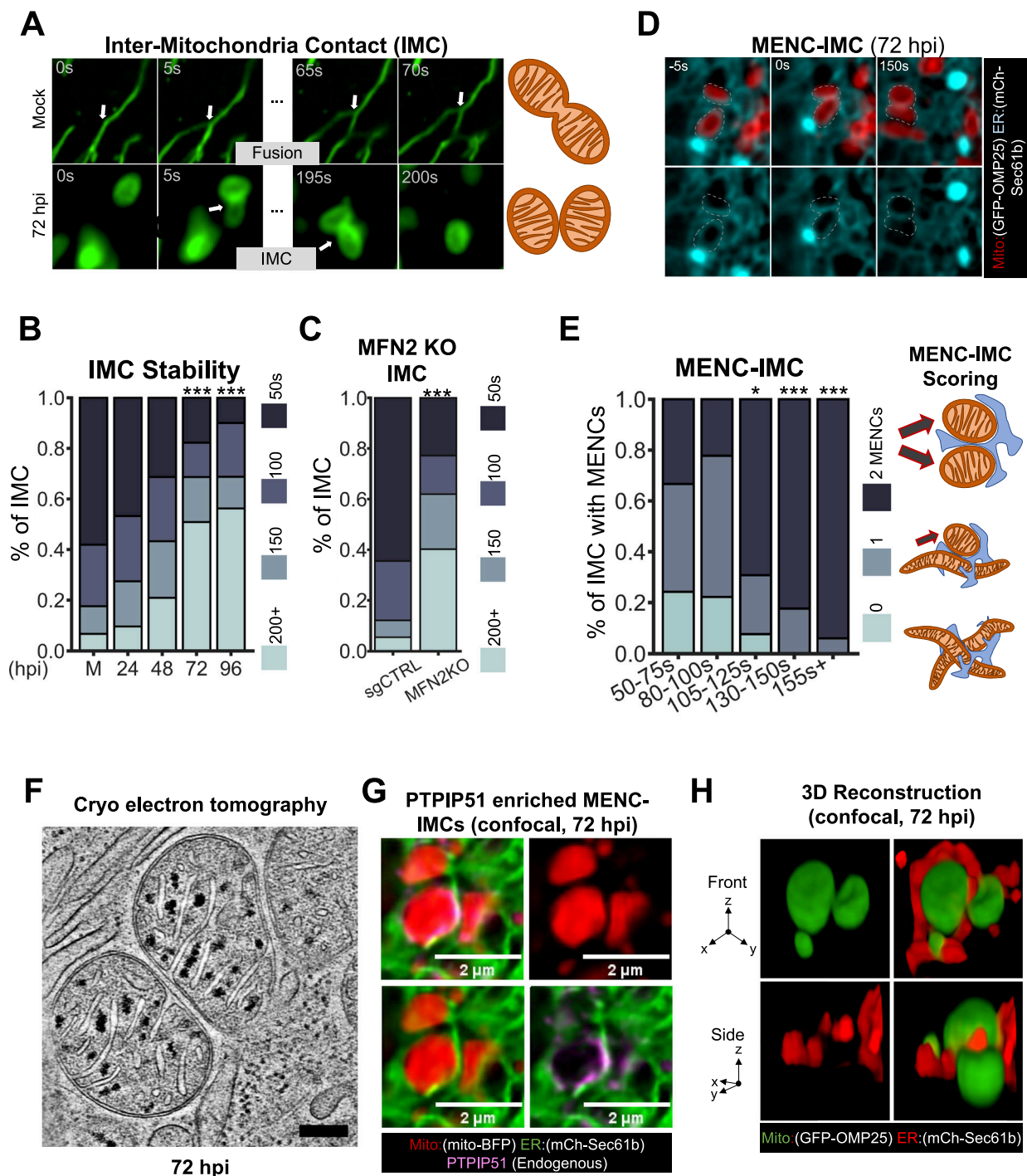
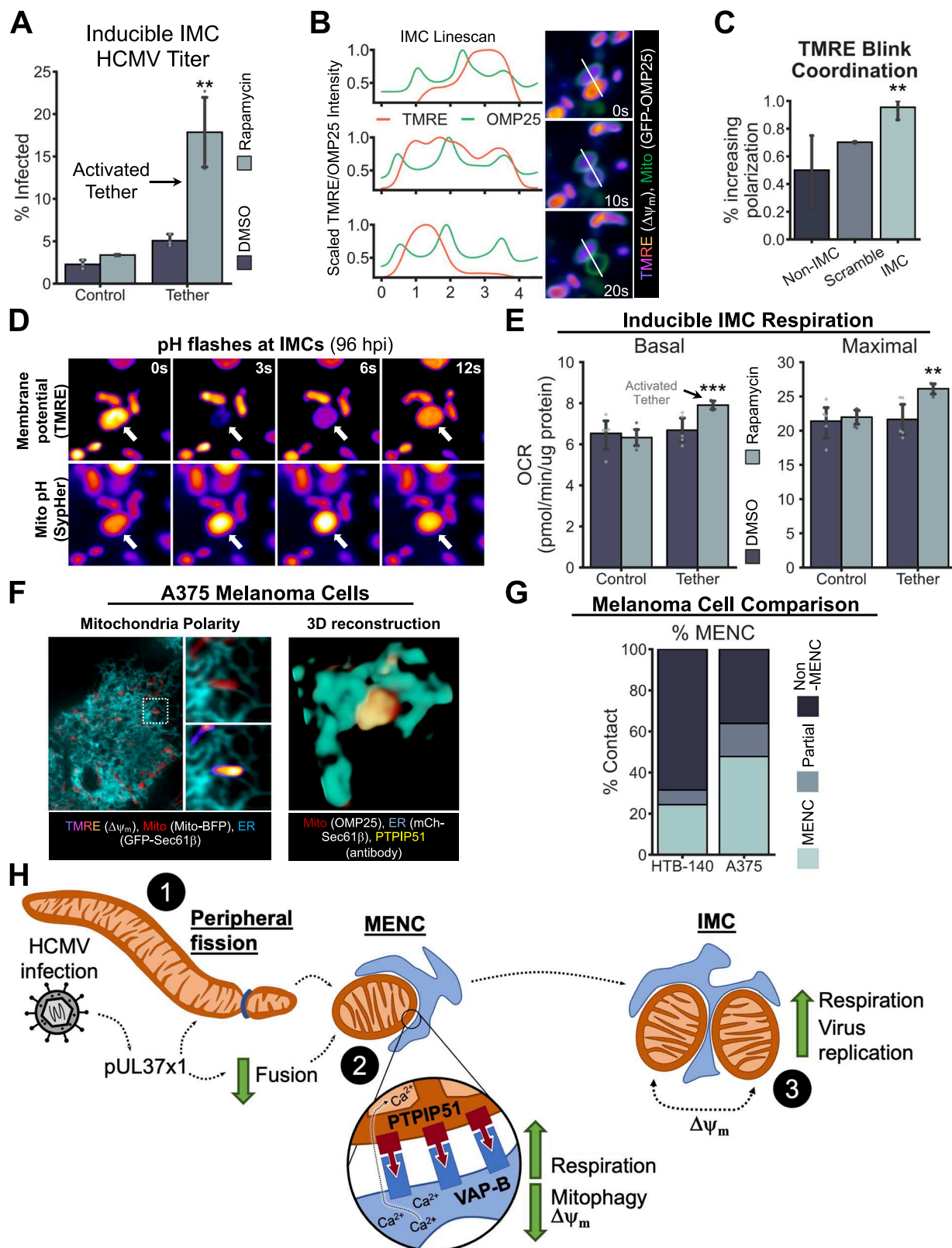


Fig. 5 | MENCs and fusion suppression stabilize inter-mitochondria contacts.

A Representative timelapses of mitochondria (OMP25) fusion in uninfected cells (top) and stable inter-mitochondria contact (IMC) in infected cells by 72 hpi (bottom) (ROI = $10 \times 10 \mu\text{m}$). **B** Quantification of IMC stability throughout HCMV replication. (Mock = 4, 48 hpi = 2, 24/72/96 hpi = 3 biological replicates; total of 400 events analyzed). **C** Quantification of MFN2 KO-induced IMC stability. ≥ 3 IMC per cell, ≥ 10 cells per condition, $n = 3$ biological replicates. Total of 182 IMCs. **D** Representative images of two mitochondria (GFP-OMP25, red) in MENCs associated with ER (mCh-Sec61b, cyan) forming a stable IMC (ROI = $4.76 \times 4.57 \mu\text{m}$). **E** Right: Cartoon representation of scoring IMC as arising from 0, 1 or 2 MENCs. Left: Quantification of whether 0, 1 or 2 mitochondria were in MENCs prior to IMC onset, binned by IMC temporal stability (10 cells per replicate; $n = 3$ biological replicates, 114 IMC across 30 cells). **F** Slice through a tomogram of HCMV-infected cell at 72 hpi showing a Mito-mito contact (whole volume shown in Supplementary

Movie S8). Scale bar is 200 nm. Representative of one biological replicate with 23 cells across two grids being selected for FIB-milling. Out of these, 6 lamella sites were successfully polished and used for cryo-ET data acquisition. In total 34 tilt series were acquired of which 27 contained mitochondria and ER in close proximity. **G** Representative microscopy showing a MENC-IMC with a PTIP51 enriched ER tubule running in between the contacting mitochondria. Scale bar is $2 \mu\text{m}$. **H** 3D reconstruction of a MENC-IMC. Top row shows a front view while the bottom row displays a side view, as indicated by the cartoons on the left. hpi hours post infection, mito mitochondria, ER endoplasmic reticulum, s seconds, M mock, MENC mitochondria-ER encapsulation, KO knockout, IMC inter-mitochondria contact. Data are presented as mean values with 95% confidence intervals. Black asterisks indicate statistical comparison to uninfected cells. * $P \leq 0.05$, ** $P \leq 0.01$, and *** $P \leq 0.001$ using a Welch's t test. Source data are provided as a Source Data file.



Next, we wanted to determine if there was any exchange of matrix components at IMCs which may be driving the coordination of their membrane potentials. Therefore, we again expressed the photoconvertible plasmid mito-Dendra2 to selectively label mitochondria³⁶. If matrix components were transferred at IMCs, when a photoconverted mitochondria (red) forms an IMC with a non-converted mitochondria (green), we would observe that the red signal would

spread to both mitochondria. However, no transfer of the red or green signals was observed following contact, indicating that the matrices of contacting mitochondria are not connected (Supplementary Fig. S9E). To determine if membrane potential coordination at IMC mitochondria is indicative of an electrochemical linkage⁸¹, we expressed the mitochondria pH-sensitive construct mito-Sypher3⁸⁴ (Sypher) concurrent with TMRE treatment. Indeed, we observed that sudden

Fig. 6 | IMC promote mitochondria bioenergetics during HCMV infection.

A Titers of HCMV infectious virions produced in cells transfected with both FKBP and FRB (Tether) or FRB and OMP25 (Control) then at 72 hpi treated with 100 nM Rapamycin or DMSO to induce mito-mito tethering (see “Methods”). Arrow indicates where the tether is activated through both FKBP and FRB expression as well as rapamycin treatment ($n = 3$ replicates). Exact P values; %Infected: Tether+Rapamycin vs. Tether+DMSO = 0.011; Tether+Rapamycin vs. Control+Rapamycin = 0.009; Tether+Rapamycin vs. Control+DMSO = 0.007. **B** Mitochondria appear to exchange membrane potential at IMC. Timelapse images (right) with line scan quantifications (left) indicate OMP25 intensity and TMRE intensity, correlated with membrane potential ($\Delta\Psi_m$). **C** Graph indicating the percent of mitochondria that are increasing their membrane potential when their partner depolarizes. Random is a control comparison to a random non-IMC mitochondria in the same cell as the IMC. Scramble is another control where the TMRE intensity is scrambled in the contacting mitochondria to determine the random frequency of depolarization-polarization alignment. ($n = 11$ depolarizations). Exact P values; % Increasing polarization: IMC vs. Non-IMC = 0.001; IMC vs. Scramble = 0.009. **D** Example of a pH flash showing concurrent mitochondria depolarization (top) and mitochondria

alkalinization (bottom). **E** Only expression of the tether (FKBP-FRB) and treatment with 100 nM Rapamycin to activate the tether (condition indicated by the arrow) results in increased basal and maximal respiration, given as oxygen consumption rate (OCR) ($n = 5$). Exact P values; Basal OCR: Tether+Rapamycin vs. Tether+DMSO = 0.040; Tether+Rapamycin vs. Control+Rapamycin = 0.0006; Tether+Rapamycin vs. Control+DMSO = 0.035; Maximal: Tether+Rapamycin vs. Tether+DMSO = 0.046; Tether+Rapamycin vs. Control+Rapamycin = 0.002; Tether+Rapamycin vs. Control+DMSO = 0.026. **F** A375 melanoma cells exhibit similar morphology to 48–72 hpi HCMV cells, displaying polarized MENC mitochondria (left) with asymmetric PTPIP51 distribution (right). **G** Left: A375 melanoma cells have a higher MENC percentage than HTB-140 cells. Exact p value; Percent MENC: A375 vs. HTB-140 = $1.025E-07$. Ten mitochondria per cell; $n = 20$ cells, total of 400 mitochondria analyzed. **H** Proposed model. $\Delta\Psi_m$ mitochondria membrane potential, hpi hours post infection, mito mitochondria, ER endoplasmic reticulum, s seconds, M mock, MENC mitochondria–ER encapsulation, IMC inter-mitochondria contact, mCh mCherry. Data are presented as mean values with 95% confidence intervals. * $P \leq 0.05$, ** $P \leq 0.01$, and *** $P \leq 0.001$ using a Welch's t test. Source data are provided as a Source Data file.

membrane potential depolarizations at IMCs during infection occurred concurrently with mitochondria alkalinization (Fig. 6D). These phenomena, termed mito flashes⁸¹, are poorly understood, particularly during virus infection, but may be a mechanism for energy conservation⁸¹. However, further experimentation would be required to link the observed flashes to altering the course of HCMV infection or impacting bulk mitochondria function. Altogether, our results show that induction of IMCs results in increased respiration and has a proviral effect during HCMV infection.

MENCs are prevalent MCSs in highly metastatic melanoma cells

Having established that mitochondria within MENCs are bioenergetically active and protected from mitophagy, we next asked whether these structures are prevalent in other disease contexts with similar metabolic shifts to HCMV. Metabolically, HCMV is similar to several cancers through instigation of a Warburg-like effect, concurrent with anaplerotic glutaminolysis and increased respiration^{15–17,85,86}. The metabolic rewiring induced by HCMV infection is thought to partially underlie the oncomodulatory capability of this virus^{87,88}. We thus turned to highly metastatic A375 melanoma cells, which are known to have fragmented mitochondria concurrent with upregulated glycolysis and OXPHOS⁸⁹. A375s have been shown to be one of the most tumor-like melanoma cell lines⁹⁰. For comparison, we also analyzed HTB-140 cells, another melanoma cell line shown to have decreased metabolism compared to A375s⁹¹. Using live-cell super-resolution imaging, we observed that mitochondria in A375 cells appear slightly more fragmented than in HTB-140 cells, at a level similar to 48–72 hpi with HCMV. Akin to this infection timepoint, we find that MENCs represent the dominant ER-mitochondria MCS in A375s, but not in HTB-140s (Fig. 6F, G). PTPIP51 localized asymmetrically at these structures in A375 cells. Furthermore, we found that MENC mitochondria were bioenergetically active in this cell line. These findings highlight MENCs and PTPIP51 as a potentially conserved structure used in diverse contexts in which mitochondria membrane potential needs to be maintained in conjunction with mitochondria fragmentation.

Discussion

Here, we report the discovery of a mechanism through which mitochondria fragmentation can lead to increased respiration (Fig. 6H). Using HCMV infection as a biological model system, we demonstrate that (1) mitochondria fragmentation through peripheral fission and suppression of fusion leads to MENC formation. (2) By 72 hpi, these peripheral progenies within MENCs exhibit suppressed mitophagy, as well as dampened membrane potential indicative of increased respiration. This requires the contribution of PTPIP51, which is also necessary for increasing OXPHOS. (3) Inhibition of fusion and MENCs

are associated with the stabilization of proviral IMCs that, when synthetically induced, lead to increased respiration. Given that we also observe prevalent MENCs in metastatic melanoma cells, we propose that MENCs represent a previously unexplored facet of disease development. Our findings indicate that MENCs may be relevant in other disease conditions that require increased respiration coupled to mitochondria fragmentation.

Through live-cell image analysis, we show that, unexpectedly, HCMV infection induces mitochondria fragmentation not through upregulation of fission, but instead through suppression of fusion. Furthermore, we show that HCMV infection controls the balance between midzone and peripheral fission, suppressing midzone and mildly upregulating peripheral fission. One question to consider is why has HCMV acquired a mechanism to induce mitochondria fragmentation? There are several aspects of mitochondria fragmentation that could benefit HCMV replication. Smaller mitochondria have increased motility, thereby allowing for their rapid localization to areas of high-energy demand^{92–95}, such as around the viral assembly complex during HCMV infection. Abundant smaller mitochondria also have increased surface area-to-volume ratio compared to fewer longer mitochondria, which would provide a larger platform for ER-mitochondria contacts.

If HCMV does require fragmentation of the mitochondria network, the follow up question is why does infection promote suppression of fusion rather than enhanced fission? First, mitochondria fusion is associated with accumulation of antiviral factors, such as MAVS, in several contexts^{96,97}. Second, enhanced mitochondria fission has been shown to promote cell death through Drp1^{4,5}. HCMV replicates over a relatively long cycle, and thus must keep the host cell alive and evade antiviral signaling for an equally long time.

Finally, why does HCMV suppress midzone fission while sustaining peripheral fission? Assuming HCMV favors smaller mitochondria, for the reasons listed above, peripheral fission would be the quickest way to achieve this, given that every round of fission produces a smaller progeny. We also find that peripheral fission is specifically linked with proviral MENC formation. In fact, it may be that the production of these smaller mitochondria is why peripheral fission is linked with MENC formation. In addition, MFF, which mediates midzone fission, has been shown to instigate MAVS clustering and activation at mitochondria⁹⁸. Peripheral mitochondria fission would avoid this form of MAVS activation through use of Fis1 instead of MFF³.

It is possible that the suppression of mitochondria fusion and the altered balance between midzone and peripheral fission are inherently linked. Kleele et al. reported the fates of two generations of mitochondria following peripheral or midzone fission³. They found that the resulting progenies from peripheral fission were less likely to subsequently undergo fusion, with only 1% of the smaller progenies

inevitably fusing. Therefore, increasing the relative rates of peripheral over midzone fission may also be sufficient to drive both mitochondria fragmentation and suppression of fusion. Furthermore, KO of MFF was shown to promote peripheral fission³. While it is unlikely that MFF is completely suppressed during HCMV infection, it may be sequestered to peroxisomes. We previously reported that pUL37x1 interacts with MFF late in infection⁷⁰ and it was recently shown that pUL37x1 induces MFF-dependent peroxisome fission⁶⁹.

It is important to note that the benefits of fragmentation listed here are only useful to HCMV replication if the smaller mitochondria in question are bioenergetically stabilized and protected from mitophagy. Both peripheral fission and increased reactive oxygen species (ROS) production¹⁶, known to occur during HCMV infection, will target mitochondria for degradation^{3,99}. We instead observe mitophagy to be decreased upon HCMV infection, suggesting that HCMV is actively suppressing it. However, this does not explain how mitochondria remain healthy, given that a regular cycle of fission, fusion, and mitophagy is important for mitochondria quality control¹. In fact, loss of mitochondria fusion and mitophagy is associated with mitochondria dysfunction in many contexts, including cancer, neurodegenerative diseases, and metabolic diseases¹⁰⁰. Therefore, HCMV-infected mitochondria must have alternative methods for dealing with the build-up of detrimental ROS associated with aged mitochondria¹⁰¹. Our findings suggest this may be a function of MENC-IMCs.

Using super-resolution microscopy and cryo-ET, we show that MENCs form preferentially following peripheral fission. We also show that suppression of mitochondria fusion is sufficient to drive MENC formation either through pUL37x1 expression or MFN2 KO. The connection between peripheral fission and MENC formation may be as simple as MENCs requiring smaller mitochondria, which are produced with peripheral fission. However, previously we showed that induction of mitochondria fragmentation through staurosporine treatment was insufficient to drive the PTPIP51 relocalization associated with MENC formation³⁰. Therefore, peripheral progenies may be actively shuttled into MENCs. Peripheral progenies are preferentially targeted for degradation, thus they would most benefit from the anti-mitophagy environment of a MENC.

By integrating live imaging with proteomics and functional metabolic assays, we show that PTPIP51 and MENCs associate with several host and viral proteins to optimize mitochondria activity. Following up on the PTPIP51 association with several autophagy-related proteins, we establish that mitophagy is decreased at MENCs. This may occur through several, not mutually exclusive, mechanisms. Increased ER-mitochondria contact is known to decrease mitophagy³⁴. Therefore, the encapsulating ER tubule of a MENC may physically block mitochondria interaction with autophagosomes. In addition, we find that the LC3 activating complex ATG5/12/16L loses its interaction with LC3 during infection, while the interaction with PTPIP51 is sustained. Thus, PTPIP51 may sequester this complex within MENCs to prevent LC3 maturation and autophagosome formation.

In alignment with the reports that HCMV infection increases TCA flux and OXPHOS^{15,16,86,102}, we further find that PTPIP51 associates with proteins regulating mitochondria metabolism. Our functional assays establish that PTPIP51 is required for increased mitochondria respiration during HCMV infection. While ETC function cannot be measured on the individual mitochondria level in situ, our Seahorse findings during PTPIP51 KD indicate that mitochondria within MENCs exhibit increased ETC function. Further suggesting that MENCs specifically display increased respiration, we find that MENC mitochondria have slightly lower membrane potential than non-MENC mitochondria, as would be indicative of proton flux toward ATP phosphorylation. Our results highlight the prominent role MENC mitochondria play in meeting the high-energy demands of HCMV replication.

Of note, PTPIP51 has also recently been established as important for lipid transfer⁷². This function fits well with our findings and could help to explain the pleiotropic functions of PTPIP51 during HCMV infection. This is particularly true of PTPIP51's known role in regulating cardiolipin, a mitochondria-enriched lipid that is necessary for the function of many mitochondria proteins¹⁰³. Further support of a tight link between MENCs and increased respiration also comes from our analysis of highly metastatic melanoma cells. Previous studies have shown that several melanoma cell lines exhibit both mitochondria fragmentation and elevated oxygen consumption when compared to non-cancerous skin cells^{24,89,91}. Our results demonstrate that highly metastatic melanoma cells exhibit prevalent MENC formation, highlighting MENCs as conserved structures in different disease states with high-energy demands.

Providing further insight into how MENCs help to maintain a healthy mitochondria population, we demonstrate that, during infection, MENCs participate in the formation of stable inter-mitochondria contacts (IMCs). In turn, IMCs display electrochemical coordination and we find their induction is proviral and increases respiration. Inter-mitochondria communication is most prevalent in cells with high-energy demands, such as heart cardiomyocytes⁸⁰. Therefore, we suggest that HCMV infection rewires mitochondria in ways that are reminiscent of cardiomyocyte strategies to meet the similarly high-energy demands of viral replication and assembly.

In summary, here we address the fundamental question of how, in certain biological contexts, mitochondrial fragmentation leads to increased respiration. This question is relevant for several critical energy-demanding pathologies, including viral infection and cancer. We report the discovery of a mechanism where a viral infection promotes peripheral mitochondrial fragmentation and then leverages ER-mitochondria and inter-mitochondria membrane contacts to stabilize and elevate bioenergetic output.

Methods

Reagents

Reagents used in this study are listed in Table 1.

Cell lines and culture

MRC5 primary human fibroblasts (ATCC CCL-171, used passages 17–27), HTB-140 melanoma cells and A375 human melanoma cells were cultured under normal conditions at 37 °C, 5% CO₂ in complete growth medium (DMEM containing high glucose and supplemented with 10% fetal bovine serum as well as penicillin and streptomycin). All cell lines used in this study were subjected to mycoplasma detection tests and further validated via microscopy analysis of cellular morphology.

Viral strains, infection, and titering

Bacterial artificial chromosomes in MRC5 fibroblasts were used to produce viral stocks of wild-type AD169 HCMV¹⁰⁴. pUL37-GFP HCMV was a gift from Dr. Thomas Shenk and was generated by BADwt AD169¹⁰⁵. ΔUL13-HCMV was described previously¹⁵. Stock titers were determined using tissue culture infectious dose (TCID₅₀), as well as immunofluorescent (IF) quantification of focus forming units/mL (FFU/mL) via staining for the HCMV immediate early protein IEL. These stocks were subsequently stored at –80 °C.

For viral infection, virus aliquots were thawed in a 37 °C water bath. The warmed virus was diluted in the proper volume of complete DMEM to achieve the desired multiplicity of infection (MOI). To ensure full infection, WT cells were infected at MOI = 3, while transfected and KD cells were infected at MOI = 5. The diluted virus was added dropwise to the plate, which was then placed in the incubator for 1 h, shaking the plate every 15 min. After 1 h, the viral media was removed, and the plate was washed twice with PBS before adding back complete DMEM.

Table 1 | Reagents used in this study

Reagent	Type	Concentration/dilution/sequence	Manufacturer
Mito-BFP	Plasmid	300 ng/mL	Addgene (Voeltz Lab) 49151
GFP-OMP25	Plasmid	125 ng/mL	Addgene (Voeltz Lab) 14150
GFP-Sec61β	Plasmid	300 ng/mL	Addgene (Rapoport Lab) 15108
mCherry-Sec61β	Plasmid	300 ng/mL	Addgene (Voeltz Lab) 49155
Mito-Dendra2	Plasmid	300 ng/mL	Addgene (Chan Lab) 55796
mtCameleon(pcDNA-4mtD3cpv)	Plasmid	250 ng/mL	Addgene (Palmer and Tsien Labs) 36323
AKAP-YFP-FRB	Plasmid	125 ng/mL	Gift (Wallace Lab)
AKAP-mRFP-FKBP	Plasmid	125 ng/mL	Gift (Wallace Lab)
mtKeima-red	Plasmid	300 ng/mL	Addgene (Davidson Lab) 56018
pUL37x1-GFP	Plasmid	150 ng/mL	Cloned
Mito-SypHer3s	Plasmid	300 ng/mL	Addgene (Belousov Lab) 108119
GW1-Mito-pHRed	Plasmid	150 ng/mL	Addgene (Yellen Lab) 31474
LC3A/B	Antibody	1:200	Cell Signaling 12741
PTPIP51	Antibody	1:750	Sigma-Aldrich HPA009975
IE1	Antibody	1:50	1B12 (Shenk Lab)
CCCP	Drug	5/20/40 μM	Cayman Chemicals 25458
TMRE	Drug	200/25 nM	Abcam Ab113852
Rapamycin	Drug	100 nM	Millipore Sigma 553210
HALT protease/phosphatase inhibitor	Drug	1x	Thermo Fisher Scientific P178446
Control siRNA (siGFP)	siRNA	GGUGUGCUGUUUGGAGGUCTT	Millipore Sigma Custom Mission siRNA
siPTPIP51	siRNA	GAAGCUAGAUGGUGGAUGAUU	Millipore Sigma Custom Mission siRNA

To quantify viral units produced during infection, at 120 h post infection (hpi), virus-containing media was collected and serially diluted (1:10–1:10,000) for infection of a reporter plate. At 24 hpi, the reporter plate was fixed using 4% paraformaldehyde (PFA) in PBS. Fixed cells were permeabilized in methanol at -20°C for 15 min and subsequently washed in PBS containing 0.1% Tween-20 (PBST). Samples were blocked in PBST containing 5% goat and human serum for 15 min prior to incubation with 1:40 mouse anti-IE1 primary antibody (Table 1) in PBST for 1 h. Cells were rinsed with PBST then washed twice with PBST for 8 min each. The secondary antibody goat anti-mouse AlexaFluor 488 and DNA dye DAPI were diluted 1:1000 and added to the cells for 45 min of incubation. Cells were again rinsed with PBST and then washed twice with PBST for 8 min and once with PBS for 8 min. Samples were imaged and percent infected cells was quantified using the Operetta imaging system (Perkin Elmer). Several different viral dilutions were used to ensure that we were not over or under-saturating with virus.

Plasmid construction and transfection

Primers were designed using snapgene to extract the pUL37x1 coding sequence from the AD169 HCMV BAC (AC146999.1)¹⁰⁴. InFusion (takara) was used to remove the LAMP1 region from a LAMP1-GFP plasmid (Addgene plasmid # 34831) then ligate UL37x1 to this region. Sanger sequencing was used to confirm a successful reaction.

DNA plasmids were combined in a 1mg:3 mL ratio with X-tremeGENE HP DNA transfection reagent (Sigma-Aldrich) and mixed in Opti-MEM (Life Technologies). The amount of DNA was optimized

for each plasmid (Table 1). This mixture was incubated at room temperature for 20 min. Meanwhile, cells (70% confluent) were washed with PBS and media was replaced with Opti-MEM. After 20 min, the transfection mixture was added dropwise to the cells and incubated for 5.5 h. Immediately after incubation, transfected cells were split into new dishes with complete media to increase transfection efficiency. Cells were treated or imaged 24–48 h post transfection (depending on the cell density). The amount of plasmid transfected varied based on the construct (see Table 1).

For induction of FRB/FKBP tethering⁸⁰, transfected cells were treated with 100 nM rapamycin or control DMSO diluted in Opti-MEM for 30 min prior to imaging. For performing a Seahorse or FFU assay on these samples, rapamycin or DMSO was instead diluted in complete growth media.

For all knockdowns (KDs) in this study, cells were grown to 65–70% confluency prior to KD. In all, 80 picomoles of siRNA oligos were used per 2 mL well of cells (~150,000 cells). siRNA was incubated in Lipofectamine RNAiMAX (Thermo Fisher Scientific) and OMEM for 5 min, according to the manufacturer protocol, before being added to cells in fresh, complete DMEM. KD cells were left for 48 h before further experiments and were not passaged during siRNA transfections. For virus infections, a fresh mix of siRNA, RNAiMAX, and OMEM was re-added to the media after the inoculation period. KDs were confirmed by western blotting.

siRNA oligos were designed in-house and purchased via Millipore Sigma (CustomsiRNA), with dT[dT] 5' caps and no modifications. siRNA oligo sequences are included in Table 1.

Light microscopy

Several instruments were used for light microscopy, including a Nikon Ti-E confocal microscope with a spinning disc module and a Nikon W1-SoRa super-resolution. In all, $\times 60$ and $\times 100$ oil-immersion objectives were used for imaging with a further $2.8\times$ SoRa magnifier used on the Nikon W1 microscope. Nikon Elements (v.5.42.02) software was used. For both live and fixed cell imaging experiments, cells were seeded on fibronectin pre-coated 35-mm glass bottom microscope dishes (MatTek). For live-cell imaging, media was changed to Opti-MEM just prior to imaging in an environmental control chamber, maintaining 37°C and $5\% \text{CO}_2$. For fixed cell imaging, cells were fixed for 20 min with 4% paraformaldehyde diluted in PBS. Samples were then washed three times with PBS prior to storage at 4°C until staining or imaging.

For immunofluorescence (IF) staining, fixed samples were permeabilized in either -20°C methanol or at room temperature PBST for 5 min. Cells were blocked in PBST containing 5% goat and human sera (Sigma). Primary antibody was then added (dilutions in Table 1) and either incubated at room temperature for 2 h or overnight at 4°C . Samples were washed three times with PBST prior to the addition of 1:2000 AlexaFluor secondary antibody (Thermo Fisher). Finally, cells were washed sequentially with PBST, PBS, and TBS and either imaged immediately or stored at 4°C for up to 2 weeks. Cells were kept out of the light for the entire staining procedure.

For live-cell video experiments, images were acquired every 5 s over a 5-min period. A minimum of 10 videos were collected per sample. For most samples, 15–20 videos were collected. Images were denoised using Nikon AR analysis software (v.5.30.05) prior to analysis either in Fiji (ImageJ v.2.14/1.54 f) or Python (v.3.7–3.11).

Individual image acquisition, and analysis

Manual quantification

Peripheral fission quantification. Cells were transfected with mito-BFP and either mock or infected with HCMV. Live-cell images were acquired as above and loaded into ImageJ for visualization. Videos were manually analyzed for fission events, defined as one mitochondrion stably and clearly splitting into two pieces. The length of the parent and progeny mitochondria was measured using a segmented line. If the length of the progeny was greater than 25% of the parent, the fission event was classified as midzone. If the length of the progeny was equal to or less than 25% of the parent then the fission event was classified as peripheral.

Mito-Dendra2 photoconversion. To individually label mitochondria for fission and IMC analyses, we expressed mito-Dendra2³⁶. This construct localizes to mitochondria and under normal conditions fluoresces green. Upon stimulation with 405 nm light, however, this construct photoconverts to red fluorescence. We performed this acquisition on a Nikon Ti-2 Spinning disc confocal microscope with a 405 nm stimulation laser. For stimulation, we drew an ROI around the mitochondria of interest and then began a live-imaging acquisition. Following the first frame of this acquisition, the selected ROI was stimulated with 20% power from the 405 nm laser with a dwell time of 5000 s . Following stimulation, photoconversion was readily visible.

Mitochondria potential quantification. Cells were transfected with GFP-OMP25 or mito-BFP and GFP-Sec61 β . Two different protocols were tested for TMRE treatment and quantification. (1) Transfected cells were treated with 200 nM TMRE dye diluted in Opti-MEM and incubated at 37°C , $5\% \text{CO}_2$ for 10 min. Live cells were then gently washed with Opti-MEM and immediately imaged as described above. To quantify the fold-change difference in mitochondria potential between the parent and progeny mitochondria, we first measured the maximum TMRE intensity^{3,66} of the parent at the fission site one frame prior to fission (5 s before). The potential of the progeny was similarly

measured as the maximum TMRE intensity at the site where the mitochondria split off one frame after fission (5 s after). TMRE intensity was measured only at the site of fission, instead of along the entire length of the mitochondria, because mitochondria can have uncoupled cristae, where different cristae have different potential in the same mitochondria^{106,107}. This phenomenon was evident upon TMRE staining, where mitochondria exhibited patches of differentially polarized cristae along their length. This was particularly observable for longer mitochondria, commonly found in uninfected MRC5 fibroblasts. (2) Cells were similarly treated with TMRE, this time with 25 nM for 20 min. Cells were then imaged as above. For analyzing these images, we drew ROIs along the length of the entire mitochondria (that was in focus) just prior to and following fission. The mean of this intensity was then calculated for each of these times. To compare how membrane potential was changed with fission, we again took the \log_2 fold change of the TMRE intensity after fission (progeny) to the intensity before fission (parent).

Mitochondria–ER encapsulations (MENC) quantification. Cells were transfected with either mito-BFP and GFP-Sec61 β or GFP-OMP25 and mCherry-Sec61 β . Live cells were imaged as described above. Images were manually quantified for MENCs, defined as stable asymmetric ER encapsulation of a mitochondria. For quantification of MENC membrane potential, these cells were also treated with TMRE as described above. TMRE intensity was measured in three encapsulated and non-encapsulated mitochondria for each cell. TMRE intensity was also normalized to mito-BFP signal to account for the differences in mitochondria size between MENC and non-MENC mitochondria.

LC3 MENC intensity. To quantify LC3 intensity for all mitochondria, independent of MENC status, we would have been able to apply our automated pipeline (see “Computational Quantification” section below); however, this system would not discern MENCs. Therefore, we manually quantified LC3 intensity to compare levels in MENC and non-MENC mitochondria. Unlike the above MENC quantification, however, this protocol is not amenable for the analysis of live cells, as it requires staining for LC3. However, analysis of over a thousand MENCs gave us confidence that we can readily discern which MENC-like structures are temporally stable given a single frame. To further ensure that most structures analyzed are MENCs, this analysis was only performed at 72 hpi, when MENCs are the dominant ER-mitochondria phenotype. Furthermore, we analyzed 10 MENCs per cells, 10 cells per replicate, 3 replicates in total, resulting in the quantification of 300 MENCs. This high number of events considered should help to dilute out false MENCs. Once a MENC-associated or non-associated mitochondria was identified, the LC3 intensity within that mitochondria was quantified using ImageJ. To account for cell-to-cell variability in LC3 intensity, 10 MENC and 10 non-MENC mitochondria were counted within the same cell, then scaled to the median of those 20 values.

Mitochondria fusion quantification. Cells were transfected with GFP-OMP25 and live imaged as described above. These videos were manually analyzed for fusion events, defined as the stable fusion of the outer mitochondria membranes. Due to the high number of fusion events in some mock cells, the maximum number of fusion events for a cell was capped at 10.

Mitochondria calcium quantification. WT cells were transfected with mitoCameleon (mtCameleon) and GW1-Mito-pHRed (mito-pHRed), as described above. Single Z-slice images were taken live in uninfected cells and across HCMV infection (24, 48, 72 hpi). Ratiometric cameleon signal was acquired via 405 nm excitation coupled with either 445 nm (CFP) or 488 nm (FRET) emission. The ratiometric mito-pHRed signal was acquired via either 445 nm or 561 nm excitation, both coupled with 565 nm emission. ROIs were drawn around 3–5 randomly selected

mitochondria per cell. Cameleon signal was quantified using Eq. (1).

$$\text{Ratio} = \frac{(FRET_{\text{int}} - FRET_{\text{background}})}{(CFP_{\text{int}} - CFP_{\text{background}})} \quad (1)$$

Mito-pHRed was quantified similarly to above, with the 561 nm excitation as the numerator and 445 nm excitation signal as the denominator. Mitochondria calcium content was then determined by normalizing the Cameleon signal to the mito-pHRed signal. This was performed to compensate for the fact that Cameleon probe intensity is impacted by pH.

Inter-mitochondria contact (IMC) stability quantification. Cells were transfected with GFP-OMP25 and live imaged as described above. Images were quantified manually by marking the initiation and dissolution of a IMC (visualized as a slight overlap of the GFP-OMP25 signal). We define IMC as lasting a minimum of 50 s and not ultimately leading to fusion. To properly perform this quantification, we only counted IMC where we observed their formation and dissolution. If the IMC was initiated in the first 100 s of the video and did not dissolve by the end of the video, it would still be counted as if it would be placed in the 200 s+ bin. For quantification of MENCs leading to IMC, mCherry-Sec61 β was also transfected. These videos were also manually analyzed by first looking for IMC, as described above. We would then note if, just prior to the IMC formation (1 frame, 5 s), 0, 1 or both mitochondria were in MENCs.

MENC-IMC quantification. Cells were transfected with GFP-OMP25 and mCherry-Sec61 β and live imaged at 72 hpi for 5 min per video, as described above. These videos were first analyzed for IMC. When a IMC was found, it was scored as beginning with 0, 1, or 2 MENCs as shown to the right of Fig. 5E.

IMC blinking quantification. Cells were transfected with ER and mitochondria markers as described above. To promote blinking, samples were imaged with increased 405 nm laser power (10% compared to 1–2%) with increased frequencies (3 s instead of 5 s intervals). Following the acquisition, samples were analyzed in Fiji ImageJ. IMCs were randomly chosen and the TMRE and mito-BFP intensity for both mitochondria in the IMC pair were quantified for 27 consecutive frames. In all, 1–2 additional mitochondria not in IMC were also quantified for the same corresponding frames. These values were subsequently analyzed in Python via the following methods. For all subsequent analyses, we normalized the TMRE intensity to OMP25 intensity and we quantified the percent TMRE change between each frame and the preceding 1–2 frames. From this we calculated the blink frequency, where we counted how many times a mitochondria had a 20% or greater decrease in membrane potential. We also calculated TMRE blink amplitude via three different metrics. We determined the average percent change, without taking the absolute value, which indicates whether cumulatively across these fluctuations if a mitochondria is increasing or decreasing its membrane potential. Second, we performed this analysis while taking the absolute value of each change, which indicates how much a mitochondria is fluctuating, independent of the sign. Finally, we determined the maximum absolute value percent change for each mitochondria trace.

To quantify blinking coordination within IMC, we first wanted to gather additional replicates. Therefore, we scanned these videos looked for additional mitochondria which are rapidly depolarizing. We used a similar approach as above but this time only quantifying 11 frames surrounding the depolarization event. In Python, we then took these additional traces and ran them through the same analysis as above. For this analysis, we also determined at what frame a mitochondria was decreasing its membrane potential by 35% or more. From

this, we are then able to score the contacting mitochondria as either increasing (1) or decreasing (0) its membrane potential during and immediately after the depolarization of its partner. From this we can calculate what percent of the time a mitochondria is increasing its membrane potential while its partner is depolarizing. To determine if this is more of a cell-wide phenomenon, independent of IMC, we also assessed the percent membrane potential change in a random non-IMC mitochondria at the same frame. In addition, to show that these events are not just randomly aligning, we also performed a scramble analysis. For this, we took the percent membrane potential trace of the contacting mitochondria (the neighbor to the mitochondria that was depolarizing) and randomly scrambled it, then assessed if the depolarization event still randomly aligned with an increase in the now scrambled contacting partner. To reduce the error, this was repeated 1000 times for each depolarization event.

pH Flashes acquisition. To visualize changes in both mitochondria pH and membrane potential we expressed mito-SypHer3 and treated with TMRE. Mito-SypHer3 is the 3rd generation of a pH-sensitive ratio-metric construct which is localized to the mitochondria matrix⁸⁴.

Computational quantification

General pipeline. For high-throughput analysis of the abundance of dyes and proteins within mitochondria, we developed a Python-based workflow largely using the skimage package. This workflow separated each image based on the different channels then either used the first frame or created maximum intensity projections from the Z-stacks. To roughly isolate individual cells within each image (each image has at least one cell but some have more) we used an Otsu thresholding with a low threshold. We then expanded these labels slightly and applied a convex hull. If objects were in close proximity, indicating that a cell was oversegmented, the ROIs were combined, and an additional convex hull was applied. Successful isolation of cells was validated manually for a random set of images from each dataset. For each cell ROI, we then applied a more stringent Otsu threshold followed by watershed to isolate the mitochondria. Successful mitochondria segmentation was also visually validated for a random set of images from each dataset. If the segmentation resulted in fewer than 10 mitochondria, the cell was discarded. We then iterate through the mitochondria ROIs, quantifying the mean, median, and maximum intensity for the channels of interest. We excluded objects that were too small or too large (0.8 μm^2 –155 μm^2). The median mitochondria intensity per cell was then measured. For each cell, on average, hundreds of mitochondria were measured. While HCMV infection resulted in an increase in the number of mitochondria, this does not impact any of the results because values per cell are calculated as the median fluorescence intensity of all mitochondria, not the sum. Python code for this pipeline is available on Mendeley Data (detailed below). Along with the published workflow is a document detailing how to run the code and dependencies, as well as a small test dataset.

LC3 intensity. Cells were first transfected with mito-BFP and mCh-Sec61 β as mitochondria and ER markers, respectively. At confluence, the cells were either infected with HCMV or collected as a mock sample. Sample collection occurred every 24 hpi until 72 hpi. Samples were collected by fixing with 4% paraformaldehyde mixed with 0.04% Glutaraldehyde in PBS for 20 min. These samples were subsequently washed three times with PBS for 5 min each prior to storage at 4 °C. Once the entire time course was collected, samples were permeabilized with 0.1% triton and stained with LC3A/B, as described above. Cells were imaged on the W1-SoRa as single Z-slices. These samples were then analyzed using the above workflow where we segmented based on the LC3 channel to isolate LC3 puncta, then quantified the mitochondria and LC3 intensity in those ROIs to determine relative LC3 concentration and contact to mitochondria. To determine if LC3

puncta were in contact with mitochondria we also performed thresholding in the mitochondria channel for each image (described above). If the mitochondria intensity inside an LC3 ROI was above this threshold, we quantified it as contacting.

Mitophagy quantification. Cells were transfected with mtKeima-red and infected with pUL37x1-GFP HCMV as described above. Z-slices were not taken for this experiment so that analysis was performed on a single plane. To increase the number of cells per image, samples were imaged using the 1× SoRa magnifier instead of the 2.8× used on the majority of images. Samples were imaged with 405 nm and 565 nm excitation both with 605 nm emission filter to quantify acidification. 488 nm excitation with 525 emission was also used to image pUL37x1-GFP. At neutral pH, mtKeima fluoresces more with 405 nm laser excitation. However, with acidification 405 nm intensity decreases which 565 nm excitation increases. Therefore we can use the ratio between 565 nm/405 nm to quantify acidification. We validated that mtKeima was not visualized in this acquisition by also imaging these channels without pUL37x1-GFP present. These images were then processed via python using the above workflow optimized for this analysis. For each isolated cell we then merged the 405 nm and 565 nm excitations to segment the mitochondria independent of the mitophagy status. Within each individual mitochondria, we quantified the median 405 nm and 565 nm excitation intensity and calculated the ratio between the two (565 nm/405 nm). We also quantified pUL37x1-GFP intensity within the convex hull for infected samples. We only analyzed cells in infected samples which met a minimum pUL37x1-GFP fluorescence intensity. Segmented mitochondria were classified as undergoing mitophagy if the 565 nm/405 nm ratio was greater than or equal to 1.

Electron cryo-tomography

Sample preparation and acquisition. MRC5 primary fibroblast cells were grown and infected on UltrAuFoil R1.2/1.3 300 mesh EM grids (Quantifoil) coated with fibronectin (Sigma). Cells were infected with pUL37x1-GFP AD169 HCMV as described above and plunge-frozen at 72 hpi in ethane/propane mixture cooled to liquid nitrogen temperature, using an automated plunger Leica EM GP2. The grids were then clipped into custom autogrids optimized for milling in an Aquilos (see below). Initially, the abundance and phenotype of infected fibroblasts was assessed by examining the GFP fluorescence signal with a Leica Cryo CLEM microscope. Based on this information, conditions for sample preparation were optimized and cells of interest were selected. Grids were loaded into Aquilos2 cryo FIB-SEM (focused ion beam scanning electron microscope) (Thermo Fisher Scientific) to prepare lamellae for subsequent cryo-ET data acquisition. These lamellae were milled at the lowest possible angles (typically 8°) and polished to a target thickness of ~200 nm using MAPS and AutoTEM software (Thermo Fisher Scientific). FIB-milled grids were loaded into a Titan Krios G3i microscope (Thermo Fisher Scientific) operated at 300 kV and equipped with a K3 direct electron detector and a post-column BioQuantum energy filter (Gatan) with a 20 eV slit. Tomographic datasets were collected using the dose-symmetric acquisition scheme¹⁰⁸ at a +/-60° tilt range with 3° increment steps starting at the milling angle of the lamella as the central slice. Tilt-series were recorded using SerialEM¹⁰⁹ at a target defocus of ~5 μm, a total fluence of 178 e⁻/Å² and a magnification of ×26,000, which corresponds to a calibrated pixel size of 3.356 Å².

Data processing. Alignment of tilt-series using metal particles on lamella surfaces as fiducial markers and subsequent reconstruction of tomograms was performed in IMOD¹¹⁰ using weighted back projection. Tomograms are shown with a binning of 4 and filtered with mtfilter in 3D using a cutoff radius of 0.05 and sigma value of 0.1. For display purposes, they were manually segmented in IMOD and additionally

filtered in 3Dmod using Fourier filter with the following parameters: low-frequency sigma of 0.005, high-frequency cutoff of 0.120, high-frequency falloff, 0.2.

Inducible tether

Cells were transfected with either AKAP1-mCherry-FRB and AKAP1-GFP-FKBP (Tether) or AKAP1-mCherry-FRB and GFP-OMP25 (Control). Tethering was induced via replacement of DMEM with media containing 100 nM rapamycin or as a control an equivalent volume of DMSO. Confirmation that this system induces tethering is shown in supplemental figure 7B. For live-cell experiments with the tether (live imaging, Seahorse), cells were treated with rapamycin or DMSO 2 h prior to the assay. For titering with this system, titering progressed as described above except, at 72 h post primary infection, the media of all four conditions was changed (Tether +/- Rap, Control +/- Rap) and replaced with media containing rapamycin or DMSO. This workflow is illustrated in supplemental figure 7C. For all tethering experiments, four conditions were used (tether + rapamycin; tether + DMSO; control + rapamycin; control + DMSO). Comparison between the two rapamycin conditions (with the tether or control expressed) was used to determine if rapamycin was influencing infection.

Seahorse assay

Oxygen consumption rate (OCR) was measured using the Seahorse XF Cell Mito Stress Test Kit (Agilent) following the manufacturer's guidelines. On the first day, transfected or KO cells were plated into a pre-fibronectin-coated Agilent XFe96 plate. The following day, the cells were infected with HCMV at MOI = 5. Forty-eight hours prior to the Seahorse assay, a 37 °C incubator was set to 0% CO₂. Twenty-four hours prior to the assay, the flux pack was hydrated with 200 μL of sterile H₂O and placed within the 0% CO₂ incubator. Two hours prior to the Seahorse assay, inducible tether samples were treated with either 100 nM rapamycin or an equivalent volume of DMSO. The water in the hydrated flux pack was then switched out for prewarmed Seahorse XF Calibrant solution and returned to the 0% CO₂ incubator for 1 h. After incubation, carbon source and drugs were loaded into the plate. In port A was a mixed carbon source containing 10 mM glucose, 1 mM pyruvate and 2 mM glutamine. Ports B, C, and D contained 2 μM oligomycin, 1 μM FCCP and 0.5 μM Rotenone/Antimycin A, respectively. This plate was then brought to the Seahorse analyzer for calibration. While calibrating, the cells were gently washed with Seahorse media and incubated in Seahorse Media at 0% CO₂ for 1 h. Immediately following incubation, the cells were taken to the analyzer where the oxygen consumption rate and extracellular acidification rates were continually analyzed following sequential carbon and drug treatment. Following completion of the assay, any media was removed from the cells and they were placed at -20 °C. Frozen cells were lysed directly in the plate in buffer containing 4% SDS. A BCA assay was then used to quantify the protein content per well for normalization purposes. Quantification of respiratory parameters non-mitochondria respiration, basal respiration, maximal respiration, proton leak ATP production and spare respiratory capacity were performed as previously¹⁵. Calculations are also shown in Supplemental Fig. 8.

Quantitative reverse-transcription PCR (RT-qPCR)

KD of PTP1B1 along with control KD were performed on 2.00 × 10⁵ MRC5 cells 48 h prior to infection. Cells were then HCMV (MOI 3 PFU/cell) or mock-infected; as described above in the transfection protocol, a second KD was performed immediately after inoculation period. For each timepoint, RNA extraction was performed using RNeasy Mini Kit (Qiagen), then cDNA was prepared using SuperScript IV First-Strand Synthesis Kit (Thermo Fisher Scientific) as per the manufacturer's instructions. Gene-specific primers (see Table 1) and the SYBR green PCR master mix (Life Technologies) were used to quantify cDNA by qPCR on the ViiA 7 Real-Time PCR Systems (Applied Biosystems).

Two-stage amplification was conducted at 95 °C for 30 s and 55 °C for 60 s for 40 cycles. Melting curves were conducted after amplification to identify samples with inefficient amplification. Relative mRNA quantities were determined using the $\Delta\Delta\text{CT}$ method with glyceraldehyde phosphate dehydrogenase (GAPDH) as an internal control. Following quantification, data were normalized by the average within each replicate.

Immunoaffinity purification

Sample collection and lysis. Cells were grown and HCMV or mock-infected in 10-cm dishes. For each timepoint, cells were harvested via scraping in cold PBS. After collection, samples were centrifuged at $1250 \times g$, washed, then centrifuged again. Prior to snap freezing in liquid nitrogen and storage at -80°C , HALT protease/phosphatase inhibitor was spiked in. Once all sample had been collected, cells were lysed for 10 min at room temperature in buffer containing 20 mM HEPES KOH pH 7.4, 110 mM potassium acetate, 2 mM MgCl_2 , 0.1% Tween-20, 0.6% TritonX, 1 μM ZnCl_2 , 1 μM CaCl_2 , 200 mM NaCl, 1 \times HALT protease/phosphatase inhibitor and Universal nuclease. Samples were further mechanically lysed via Polytron treatment on ice.

Bead conjugation and immunoaffinity purification. We resuspended and thoroughly washed Pierce magnetic protein A/G beads (88802, Thermo Fisher Scientific) in a bead washing buffer (same components as lysis buffer without NaCl, HALT or nuclease). We then incubated 5 μg of IgG, PTPIP51 or ATG12 antibody with 20 μL of beads for 1 h at either at room temperature, for PTPIP51 IP-MS, or at 4 °C, for ATG12. Following incubation, samples were again washed with the bead washing buffer. Lysate was added to the pre-conjugated beads and incubated for 1 h at either room temperature or 4 °C. Samples were again washed first with bead washing buffer then with water. Finally, the samples were eluted with elution buffer (106 mM Tris HCl, 141 mM Tris Base, 2% LDS, 0.5 mM EDTA) at 70 °C for 10 min and on a room temperature TOMY shaker for 10 min. Samples were immediately prepped for mass spectrometry (DDA and PRM) following elution.

Mass spectrometry

Sample prep for MS analysis. Samples were prepared as described previously³⁰. Samples were first reduced and alkylated via the addition of 25 mM TCEP and 50 mM chloroacetamide at 70 °C for 20 min, then acidified via treatment with 1.2% phosphoric acid. To extract proteins, we used Protifi S-Trap micro spin columns with trypsin digestion for 1 h at 47 °C. Following trypsinization, for samples destined for Q-Exactive quantification, the resultant peptides were resuspended in 1% formic acid/acetonitrile to a final concentration of 0.75 $\mu\text{g}/\mu\text{L}$ and loaded onto the instrument for analysis. For samples run on the TIMS ToF Ultra, peptides were resuspended in 0.1% formic acid and 4% acetonitrile to a final concentration of 0.1 $\mu\text{g}/\mu\text{L}$.

Selection of PRM peptide library. Several peptides quantified in this study were validated in previous publications³⁰. For peptides not already optimized, peptide isolation lists were developed using Skyline (v.23.1). We searched for signature peptides that were tryptic, 6–30 amino acids in length, and only contained carbamidomethyl cysteines as possible modifications. In addition, we searched MassIVE database for commonly identified peptides for each protein to further narrow down our search. We included transition ions with 2–3 precursor charges, 1–2 ion charges, and y and b ions. We also instituted a library match tolerance of 0.5 m/z and a method match tolerance of 0.055 m/z with full scan setting of 15,000 resolving power at 200 m/z for MS1 filtering and 30,000 resolving power at 200 m/z for MS2 filtering.

Initially, we chose 6–8 peptides for each protein and performed DDA alongside previously verified peptides. We uploaded the DDA-MS

RAW files first into Proteome Discoverer (v.2.4), to ID peptide spectra, then into Skyline. Based on the identified peptides, we created a retention time calculator to schedule runs for the previously unidentified peptides. We were then able to exclude peptides based on their mass error (≤ 10 ppm) and whittle the list down to 2–4 peptides per protein.

MS data acquisition (Q-exactive). Samples were analyzed via nano-liquid chromatography–mass spectrometry (LC-MS/MS) with a Dionex Ultimate 3000 nanoRSLC coupled to a Thermo Q-Exactive HF orbitrap mass spectrometer. In total, 2 μL of 0.75 $\mu\text{g}/\mu\text{L}$ sample (1.5 μg total) was injected into a 25 cm EASY-Spray HPLC column and separated over a 60-min (parallel reaction monitoring, PRM) or 120-min gradient (Data-dependent acquisition, DDA). The gradient consisted of 0–35% mobile phase 0.1% formic acid to 0.1% formic acid in 97% acetonitrile. For PRM, peptide isolation lists, as described above, were loaded into the instrument method and conducted with targeted MS2 scans. The specifications of these scans are as follows, 120,000 resolution, AGC target 5e5, max inject time of 200 ms, isolation window of 1.2 m/z and normalized collision energy of 27. For DDA, we used the Top 20 full MS to dd-MS2 scan method. Full MS scans were as follows, 60,000 resolution, AGC target resolution of 3e6, max inject time of 30 ms, and a scan range of 350–1500 m/z . The dd-MS2 scans had 15,000 resolution, AGC target of 1e5, max inject time of 42 ms, isolation window of 1.2 m/z and a normalized collision energy of 28. Samples were run using Thermo Xcalibur v.4.6.67.17.

MS data acquisition (TIMS ToF Ultra). Data-independent acquisition (DIA) analysis was performed via nano-liquid chromatography–mass spectrometry (LC-MS/MS) with a NanoElute 2 LC system coupled to a Bruker TIMS ToF Ultra mass spectrometer. This analysis was performed for the UL37 expression experiments as well as for the quantification of OPA1 and MFN1/2 abundances across HCMV infection. 1 μL of 0.1 $\mu\text{g}/\mu\text{L}$ sample (100 ng total) was injected into a PepSep C18 25 cm \times 75 μm column with a 150 μm inner diameter. The sample was then separated over a 30-min gradient using the default Bruker gradient with mobile phase of 0.1% formic acid to 0.1% formic acid in 99.9% acetonitrile with a flow rate of 250 nL/min. 10 μm emitter was used on the instrument. The resolution of the instrument is 45,000. DIA was performed using a scan range of 100–1700 m/z and a mobility ($1/K_0$) range of 0.65–1.46 Vs/cm^2 with a 50 ms ramp time. Three groups of 16 DIA windows were set spanning the mobility and m/z range, using the default Bruker window ranges given the above parameters. Estimated cycle time of 0.95 s. Collision energy was linearly scaled to the ion mobility ranging from 20 eV collision energy at 0.6 Vs/cm^2 to 59 eV at 1.6 Vs/cm^2 . Samples were run using BPS v2024b.

IP-MS data analysis. Following data acquisition, we exported the MS RAW data files and loaded them directly into Proteome Discoverer 2.4 (Thermo Fisher) with FASTA files containing human and HCMV AD169 protein sequences, as well as common contaminants. We loaded all biological replicates, timepoints and conditions concurrently for direct comparison and more accurate quantitation of P values. For our processing workflow, we first performed offline mass recalibration and label-free MS1 quantification using the Spectrum Files RC and Minora Feature Detector nodes. The MS/MS spectra were then analyzed via Sequest HT which uses forward and reverse searches to calculate the false discovery rate (FDR). During this analysis we performed a fully tryptic search allowing for two missed cleavages, precursor mass tolerance of 10 ppm, and fragment mass tolerance of 0.1 Da. In terms of modifications, we allowed dynamic methionine oxidation, phosphorylation of serine, threonine, and tyrosine, deamidation of asparagine, loss of methionine plus acetylation on the protein N-terminus as well as static carbamidomethylation. Finally, the percolator node was used to validate the spectra. Proteome Discoverer then created consensus files

for each dataset, filtering for high-confidence peptides with protein and peptide annotations. During this analysis we restricted our results to proteins with a minimum of two unique peptides, using only unique or razor peptides for quantification. The results were then exported out of Proteome Discoverer as a single Excel file. Through this analysis, we identified 2034 proteins.

We qualified unique interactors as having a *P* value (calculated by Proteome Discover) less than 0.05 and a Log₂ fold change over the paired IgG control of at least 2, for at least one timepoint. For viral protein interactions, a minimum Log₂ fold-change cutoff of 1 was used with the same *P* value restrictions. These constraints identified ~150 interactors. Given the large shift in PTPIP51 abundance across infection (~6× increase), we found that bait normalization strongly biased protein abundance toward mock and 24 hpi, when PTPIP51 abundance was low. Therefore, we instead normalized to the median abundance of all ~2000 proteins for each timepoint. Validating this approach, when normalized in this way, we find that the PTPIP51 interaction with pUL37x1 shows a higher correlation and a lower Euclidean distance to a previous study which performed pUL37x1-GFP IP-MS, then when bait normalization was performed (Supplementary Fig. S5B). Finally, for direct comparison between proteins, we scaled each timepoint for each protein to the mean abundance across all timepoints for that protein. Full results are provided in Supplementary Data 1.

Clustering was performed in Python via the sci-kit learn module KMeans with *n_clusters* = 4 and *random_state* = 0 for parameters. GO-term analysis was performed using the statistical overrepresentation tool in PantherDB.

PRM analysis. For analysis of PRM data, we loaded MS RAW files directly into Skyline for visualization of peptide spectra. Peaks were selected through comparison to an existing library of previously identified spectra as well as through mass tolerance thresholding (*ppm* ≤ 10). Each peptide was quantified based on the 1–3 most intense fragment ions across all samples. Raw peptide abundance results were then exported into an excel file. Peptides were first selected based on whether they were detected for all timepoints. Specificity of interaction was quantified based on Log₂ fold change over IgG control. For mock and 24 hpi samples this was in comparison to mock IgG and for 48–96 hpi samples this was compared to 96 hpi IgG. Each peptide was required to have a minimum of two timepoints with Log₂ fold change over IgG control of 1 or higher. In addition, at least one of the timepoints passing this threshold was required to be 72 hpi, given our specific interest in PTPIP51 interactions at this timepoint. Based on these results, we further analyzed proteins with a minimum of two valid peptides. Peptide abundances were normalized based on the median abundance of each timepoint across all 200 peptides. Validating this method, we find that PTPIP51 interactions with pUL37x1 (previously shown by pUL37x1-GFP IP-MS) and VAP-B (previously shown by a proximity ligation assay) follow similar temporal trends to previous studies. Finally, we scaled each peptide abundance to the 24 hpi abundance of that peptide.

We followed a similar workflow for analysis of the ATG12 IP samples by PRM. The main difference being that since ATG12 does not exhibit the same major change in abundance as PTPIP51, we were able to normalize to MS1 intensities for each injection. MS1 average intensities were quantified by RawMeat (Vast Scientific).

DIA analysis. For DIA analysis raw.d files were uploaded into DIA-NN (v.1.8.1)³³ using the following settings. An in silico spectral library was generated via DIA-NN using a FASTA files of the human and HCMV proteome. 1 Missed cleavage was allowed as well as N-terminal M excision and C carbamidomethylation. Peptide lengths within 7–30 amino acids and a precursor charge range of 1–4 was allowed. Precursor *m/z* range and fragment *m/z* range were set to 300–1800 and

200–1800 *m/z*, respectively. Mass accuracy (MS1 and MS2) was automatically assigned via DIA-NN based on the samples. Each experiment was analyzed altogether with match between runs (MBR). Protein inferences were heuristic from the FASTA protein names. Double-pass mode for the neural network classifier was turned on using a high-precision quantification strategy. The unique genes and stats outputs from DIA-NN were uploaded into Python for further analysis. Protein quantifications for each timepoint were normalized to the total MS1 intensity of their injection. For the OPA1 peptide analysis, the Uniprot OPA1 isoform 1 sequence was used to map each peptide to its location along the protein.

Statistics and reproducibility

Plotting and statistical analysis were performed using the Welch's *t* test from the Python math module (`stats.ttest_ind(equal_var = False)`) unless otherwise stated. Error bars displayed were quantified using Seaborn and indicate 95% confidence intervals. The number of replicates, including how many objects (cells, mitochondria e.g.) per replicate, are indicated in the figure legends as well as in Supplementary Data 2. Statistical significance is displayed in figures via asterisks: **P* < 0.05, ***P* < 0.01, and ****P* < 0.001. Black asterisks indicate statistical comparison to uninfected cells, while green asterisks indicate comparison between conditions at the same timepoint. Exact *P* values are provided in figure legends and in Supplementary Data 2. Source data are provided as a Source Data file. For images displayed that were not quantified (Figs. 3c, d, j; 4e, Sf, g), each experiment was repeated at least three times independently observing similar trends.

Reporting summary

Further information on research design is available in the Nature Portfolio Reporting Summary linked to this article.

Data availability

The MS DDA proteomics data generated in this study have been deposited in ProteomeXchange using the PRIDE repository database under accession code [PXD038330](https://proteomexchange.org/data/10.1038/s41467-024-51680-4). The normalized PTPIP51 IP-MS data generated in this study are provided in the Supplementary Data/Source Data file. The targeted MS, DIA, and PTPIP51 KD MS data used in this study are available in the Panorama public database [https://panoramaweb.org/Princeton%20University%20-%20Cristea%20Lab/PTPIP51_MCS/project-begin.view]. Source data are provided with this paper.

Code availability

Python code is available on Mendeley Data and can be accessed under the title “Segmentation and quantification of mtkeima microscopy” and <https://doi.org/10.17632/94gvtv9shf.2> here. Along with the published workflow is a document detailing how to run the code and dependencies, as well as a small test dataset.

References

1. Twig, G., Hyde, B. & Shirihai, O. S. Mitochondrial fusion, fission and autophagy as a quality control axis: the bioenergetic view. *Biochimica et. Biophysica Acta (BBA) Bioenerg.* **1777**, 1092–1097 (2008).
2. Pernas, L. & Scorrano, L. Mito-morphosis: mitochondrial fusion, fission, and cristae remodeling as key mediators of cellular function. *Annu. Rev. Physiol.* **78**, 505–531 (2016).
3. Kleele, T. et al. Distinct fission signatures predict mitochondrial degradation or biogenesis. *Nature* **593**, 435 (2021).
4. Estaquier, J. & Arnoult, D. Inhibiting Drp1-mediated mitochondrial fission selectively prevents the release of cytochrome c during apoptosis. *Cell Death Differ.* **14**, 1086–1094 (2007).

5. Tanaka, A. & Youle, R. J. A chemical inhibitor of DRP1 uncouples mitochondrial fission and apoptosis. *Mol. Cell* **29**, 409–410 (2008).
6. Yang, L. et al. Mitochondrial fusion provides an “initial metabolic complementation” controlled by mtDNA. *Cell. Mol. Life Sci.* **72**, 2585–2598 (2015).
7. Zhang, L., Qin, Y. & Chen, M. Viral strategies for triggering and manipulating mitophagy. *Autophagy* **14**, 1665–1673 (2018).
8. Khan, M., Syed, G. H., Kim, S. J. & Siddiqui, A. Mitochondrial dynamics and viral infections: a close nexus. *Biochimica et. Biophysica Acta Mol. Cell Res.* **1853**, 2822–2833 (2015).
9. Barbier, V., Lang, D., Valois, S., Rothman, A. L. & Medin, C. L. Dengue virus induces mitochondrial elongation through impairment of Drp1-triggered mitochondrial fission. *Virology* **500**, 149–160 (2017).
10. Kim, S. J. et al. Virus disrupts mitochondrial dynamics: induces fission and mitophagy to attenuate apoptosis. *PLoS Pathog.* **9**, e1003722 (2013).
11. Ripoli, M. et al. Virus-linked mitochondrial dysfunction promotes hypoxia-inducible factor 1 α -mediated glycolytic adaptation. *J. Virol.* **84**, 647–660 (2010).
12. Kim, S. J. et al. Hepatitis C virus triggers mitochondrial fission and attenuates apoptosis to promote viral persistence. *Proc. Natl. Acad. Sci. USA* **111**, 6413–6418 (2014).
13. Goldmacher, V. S. vMIA, a viral inhibitor of apoptosis targeting mitochondria. *Biochimie* **84**, 177–185 (2002).
14. McCormick, A. L., Smith, V. L., Chow, D. & Mocarski, E. S. Disruption of mitochondrial networks by the human cytomegalovirus UL37 gene product viral mitochondrion-localized inhibitor of apoptosis. *J. Virol.* **77**, 631–641 (2003).
15. Betsinger, C. N. et al. The human cytomegalovirus protein pUL13 targets mitochondrial cristae architecture to increase cellular respiration during infection. *Proc. Natl. Acad. Sci. USA* **118**, 2101675118 (2021).
16. Combs, J. A. et al. Human cytomegalovirus alters host cell mitochondrial function during acute infection. *J. Virol.* **94**, 1–19 (2019).
17. Kaarbø, M. et al. Human cytomegalovirus infection increases mitochondrial biogenesis. *Mitochondrion* **11**, 935–945 (2011).
18. Rådestad, A. F. et al. Impact of human cytomegalovirus infection and its immune response on survival of patients with ovarian cancer. *Transl. Oncol.* **11**, 1292–1300 (2018).
19. Kuo, C. P. et al. Detection of cytomegalovirus reactivation in cancer patients receiving chemotherapy. *Clin. Microbiol. Infect.* **14**, 221–227 (2008).
20. Youssry, S., Hussein, A., Ramadan, R., Alkarmouty, A. & Elsheredy, A. The association of human cytomegalovirus with biomarkers of inflammation and immune activation in breast cancer. *Breast Dis.* **41**, 229–239 (2022).
21. Simanek, A. M., Dowd, J. B., Pawelec, G., Melzer, D. & Dutta, A. Seropositivity to cytomegalovirus, inflammation, all-cause and cardiovascular disease-related mortality in the United States. *PLoS ONE* **6**, e16103 (2011).
22. Du, Y., Zhang, G. & Liu, Z. Human cytomegalovirus infection and coronary heart disease: a systematic review. *Viol. J.* **15**, 31 (2018).
23. Eryol, N. K. et al. Are the high levels of cytomegalovirus antibodies a determinant in the development of coronary artery disease? *Int. heart J.* **46**, 205–209 (2005).
24. Kumar, P. R., Moore, J. A., Bowles, K. M., Rushworth, S. A. & Moncrieff, M. D. Mitochondrial oxidative phosphorylation in cutaneous melanoma. *Br. J. Cancer* **124**, 115–123 (2020).
25. Green, K., Brand, M. D. & Murphy, M. P. Prevention of mitochondrial oxidative damage as a therapeutic strategy in diabetes. *Diabetes* **53**, S110–S118 (2004).
26. Holmström, M. H., Iglesias-Gutierrez, E., Zierath, J. R. & Garcia-Roves, P. M. Tissue-specific control of mitochondrial respiration in obesity-related insulin resistance and diabetes. *Am. J. Physiol. Endocrinol. Metab.* **302**, 731–739 (2012).
27. Yu, T., Robotham, J. L. & Yoon, Y. Increased production of reactive oxygen species in hyperglycemic conditions requires dynamic change of mitochondrial morphology. *Proc. Natl. Acad. Sci. USA* **103**, 2653–2658 (2006).
28. Scorrano, L. et al. Coming together to define membrane contact sites. *Nat. Commun.* **10**, 1287 (2019).
29. Prinz, W. A., Toulmay, A. & Balla, T. The functional universe of membrane contact sites. *Nat. Rev. Mol. Cell Biol.* **21**, 7–24 (2019).
30. Cook, K. C., Tsopurashvili, E., Needham, J. M., Thompson, S. R. & Cristea, I. M. Restructured membrane contacts rewire organelles for human cytomegalovirus infection. *Nat. Commun.* **13**, 4720 (2022).
31. Friedman, J. R. et al. ER tubules mark sites of mitochondrial division. *Science* **334**, 358–362 (2011).
32. Korobova, F., Ramabhadran, V. & Higgs, H. N. An actin-dependent step in mitochondrial fission mediated by the ER-associated formin INF2. *Science* **339**, 464–467 (2013).
33. De Vos, K. J. et al. VAPB interacts with the mitochondrial protein PTPIP51 to regulate calcium homeostasis. *Hum. Mol. Genet.* **21**, 1299–1311 (2012).
34. Gomez-Suaga, P. et al. The ER-mitochondria tethering complex VAPB-PTPIP51 regulates autophagy. *Curr. Biol.* **27**, 371–385 (2017).
35. Mórotz, G. M. et al. The PTPIP51 coiled-coil domain is important in VAPB binding, formation of ER-mitochondria contacts and IP3 receptor delivery of Ca²⁺ to mitochondria. *Front. Cell Dev. Biol.* **10**, 920947 (2022).
36. Pham, A. H., McCaffery, J. M. & Chan, D. C. Mouse lines with photo-activatable mitochondria to study mitochondrial dynamics. *Genes* **50**, 833–843 (2012).
37. Goldmacher, V. S. et al. A cytomegalovirus-encoded mitochondria-localized inhibitor of apoptosis structurally unrelated to Bcl-2. *Proc. Natl. Acad. Sci. USA* **96**, 12536–12541 (1999).
38. Song, Z., Chen, H., Fiket, M., Alexander, C. & Chan, D. C. OPA1 processing controls mitochondrial fusion and is regulated by mRNA splicing, membrane potential, and Yme1L. *J. Cell Biol.* **178**, 749–755 (2007).
39. Ishihara, N., Fujita, Y., Oka, T. & Mihara, K. Regulation of mitochondrial morphology through proteolytic cleavage of OPA1. *EMBO J.* **25**, 2966–2977 (2006).
40. Sood, A. et al. A Mitofusin-2-dependent inactivating cleavage of Opa1 links changes in mitochondria cristae and ER contacts in the postprandial liver. *Proc. Natl. Acad. Sci. USA* **111**, 16017–16022 (2014).
41. Anand, R. et al. The i-AAA protease YME1L and OMA1 cleave OPA1 to balance mitochondrial fusion and fission. *J. Cell Biol.* **204**, 919–929 (2014).
42. Lee, H., Smith, S. B. & Yoon, Y. The short variant of the mitochondrial dynamin OPA1 maintains mitochondrial energetics and cristae structure. 2017. *J. Biol. Chem.* **292**, 7115–7130 (2017).
43. Lee, H., Smith, S. B., Sheu, S. S. & Yoon, Y. The short variant of optic atrophy 1 (OPA1) improves cell survival under oxidative stress. *J. Biol. Chem.* **295**, 6543–6560 (2020).
44. Hayajneh, W. A. et al. The sequence and antiapoptotic functional domains of the human cytomegalovirus UL37 exon 1 immediate early protein are conserved in multiple primary strains. *Virology* **279**, 233–240 (2001).
45. Reboredo, M., Greaves, R. F. & Hahn, G. Human cytomegalovirus proteins encoded by UL37 exon 1 protect infected fibroblasts against virus-induced apoptosis and are required for efficient virus replication. *J. Gen. Virol.* **85**, 3555–3567 (2004).

46. Poncet, D. et al. Cytopathic effects of the cytomegalovirus-encoded apoptosis inhibitory protein vMIA. *J. Cell Biol.* **174**, 985–996 (2006).
47. Sharon-Friling, R., Goodhouse, J., Colberg-Poley, A. M. & Shenk, T. Human cytomegalovirus pUL37x1 induces the release of endoplasmic reticulum calcium stores. *Proc. Natl. Acad. Sci. USA* **103**, 19117–19122 (2006).
48. Taisne, C. et al. Human cytomegalovirus hijacks the autophagic machinery and LC3 homologs in order to optimize cytoplasmic envelopment of mature infectious particles. *Sci. Rep.* **9**, 1–13 (2019).
49. Kim, H. J., Lee, Y., Lee, S. & Park, B. HCMV-encoded viral protein US12 promotes autophagy by inducing autophagy flux. 2023. *Biochem. Biophys. Res. Commun.* **654**, 94–101 (2023).
50. Zimmermann, C. et al. Autophagy interferes with human cytomegalovirus genome replication, morphogenesis, and progeny release. *Autophagy* **17**, 779–795 (2021).
51. Clark, A. E., Sabalza, M., Gordts, P. L. S. M. & Spector, D. H. Human cytomegalovirus replication is inhibited by the autophagy-inducing compounds trehalose and SMER28 through distinctively different mechanisms. *J. Virol.* **92**, 2015–2032 (2018).
52. Belzile, J.-P. et al. Trehalose, an mTOR-independent inducer of autophagy, inhibits human cytomegalovirus infection in multiple cell types. *J. Virol.* **90**, 1259–1277 (2016).
53. Chaumorcél, M. et al. The human cytomegalovirus protein TRS1 inhibits autophagy via its interaction with beclin 1. *J. Virol.* **86**, 2571–2584 (2012).
54. Jin, M. & Klionsky, D. J. Regulation of autophagy: modulation of the size and number of autophagosomes. *FEBS Lett.* **588**, 2457–2463 (2014).
55. Sun, N. et al. A fluorescence-based imaging method to measure in vitro and in vivo mitophagy using mt-Keima. *Nat. Protoc.* **12**, 1576–1587 (2017).
56. Yamano, K. et al. Endosomal Rab cycles regulate Parkin-mediated mitophagy. *eLife* **7**, e31326 (2018).
57. Rusilowicz-Jones, E. V. et al. USP30 sets a trigger threshold for PINK1–PARKIN amplification of mitochondrial ubiquitylation. *Life Sci. Alliance* **3**, e202000768 (2020).
58. Hoshino, A. et al. The ADP/ATP translocase drives mitophagy independent of nucleotide exchange. *Nature* **575**, 375–379 (2019).
59. Zhu, Y. et al. Modulation of serines 17 and 24 in the LC3-interacting region of Bnip3 determines pro-survival mitophagy versus apoptosis. *J. Biol. Chem.* **288**, 1099–1113 (2013).
60. Isler, J. A., Maguire, T. G. & Alwine, J. C. Production of infectious human cytomegalovirus virions is inhibited by drugs that disrupt calcium homeostasis in the endoplasmic reticulum. *J. Virol.* **79**, 15388–15397 (2005).
61. Palmer, A. E. et al. Ca²⁺ indicators based on computationally redesigned calmodulin-peptide pairs. *Chem. Biol.* **13**, 521–530 (2006).
62. Palmer, A. E. & Tsien, R. Y. Measuring calcium signaling using genetically targetable fluorescent indicators. *Nat. Protoc.* **1**, 1057–1065 (2006).
63. Tantama, M., Hung, Y. P. & Yellen, G. Imaging intracellular pH in live cells with a genetically encoded red fluorescent protein sensor. *J. Am. Chem. Soc.* **133**, 10034–10037 (2011).
64. Greotti, E. et al. mCerulean3-basedameleon sensor to explore mitochondrial Ca²⁺ dynamics in vivo. *iScience* **16**, 340–355 (2019).
65. Liberman, E. A., Topaly, V. P., Tsofin, L. M., Jasaitis, A. A. & Skulachev, V. P. Mechanism of coupling of oxidative phosphorylation and the membrane potential of mitochondria. *Nature* **222**, 1076–1078 (1969).
66. Crowley, L. C., Christensen, M. E. & Waterhouse, N. J. Measuring mitochondrial transmembrane potential by TMRE staining. *Cold Spring Harb. Protoc.* **2016**, pdb.prot087361 (2016).
67. Alwine, J. C. The human cytomegalovirus assembly compartment: a masterpiece of viral manipulation of cellular processes that facilitates assembly and egress. *PLoS Pathog.* **8**, e1002878 (2012).
68. Mavinakere, M. S. & Colberg-Poley, A. M. Dual targeting of the human cytomegalovirus UL37 exon 1 protein during permissive infection. *J. Gen. Virol.* **85**, 323–329 (2004).
69. Ferreira, A. R. et al. Human cytomegalovirus vMIA inhibits MAVS oligomerization at peroxisomes in an MFF-dependent manner. *Front. Cell Dev. Biol.* **10**, 871977 (2022).
70. Federspiel, J. D. et al. Mitochondria and peroxisome remodeling across cytomegalovirus infection time viewed through the lens of inter-ViSTA. *Cell Rep.* **32**, 107943 (2020).
71. Santel, A. & Fuller, M. T. Control of mitochondrial morphology by a human mitofusin. *J. cell Sci.* **114**, 867–874 (2001).
72. Yeo, H. K. et al. Phospholipid transfer function of PTPIP51 at mitochondria-associated ER membranes. *EMBO Rep.* **22**, e51323 (2021).
73. Dietel, E. et al. Crosstalks of the PTPIP51 interactome revealed in Her2 amplified breast cancer cells by the novel small molecule LDC3/Dynarrestin. *PLoS ONE* **14**, e0216642 (2019).
74. Tanida, I., Tanida-Miyake, E., Komatsu, M., Ueno, T. & Kominami, E. Human Apg3p/Aut1p homologue is an authentic E2 enzyme for multiple substrates, GATE-16, GABARAP, and MAP-LC3, and facilitates the conjugation of hApg12p to hApg5p. *J. Biol. Chem.* **277**, 13739–13744 (2002).
75. Hanada, T. et al. The Atg12–Atg5 conjugate has a novel E3-like activity for protein lipidation in autophagy. *J. Biol. Chem.* **282**, 37298–37302 (2007).
76. Szabadkai, G. et al. Chaperone-mediated coupling of endoplasmic reticulum and mitochondrial Ca²⁺ channels. *J. Cell Biol.* **175**, 901–911 (2006).
77. Tang, J. X., Thompson, K., Taylor, R. W. & Oláhová, M. Mitochondrial OXPHOS biogenesis: co-regulation of protein synthesis, import, and assembly pathways. *Int. J. Mol. Sci.* **21**, 1–32 (2020).
78. Stephan, T. et al. MICOS assembly controls mitochondrial inner membrane remodeling and crista junction redistribution to mediate cristae formation. *EMBO J.* **39**, 1–24 (2020).
79. Ott, C. et al. Sam50 functions in mitochondrial intermembrane space bridging and biogenesis of respiratory complexes. *Mol. Cell Biol.* **32**, 1173–1188 (2012).
80. Picard, M. et al. Trans-mitochondrial coordination of cristae at regulated membrane junctions. *Nat. Commun.* **6**, 1–8 (2015).
81. Santo-Domingo, J., Giacomello, M., Poburko, D., Scorrano, L. & Demarex, N. OPA1 promotes pH flashes that spread between contiguous mitochondria without matrix protein exchange. *EMBO J.* **32**, 1927–1940 (2013).
82. Wong, Y. C., Peng, W. & Krainc, D. Lysosomal regulation of inter-mitochondrial contact fate and motility in Charcot-Marie-Tooth type 2. *Dev. Cell* **50**, 339–354.e4 (2019).
83. Cao, Y. P. & Zheng, M. Mitochondrial dynamics and inter-mitochondrial communication in the heart. *Arch. Biochem. Biophys.* **663**, 214–219 (2019).
84. Ermakova, Y. G. et al. SypHer3s: a genetically encoded fluorescent ratiometric probe with enhanced brightness and an improved dynamic range. *Chem. Commun.* **54**, 2898–2901 (2018).
85. Chambers, J. W., Maguire, T. G. & Alwine, J. C. Glutamine metabolism is essential for human cytomegalovirus infection. *J. Virol.* **84**, 1867–1873 (2010).

86. Munger, J. et al. Systems-level metabolic flux profiling identifies fatty acid synthesis as a target for antiviral therapy. *Nat. Biotechnol.* **26**, 1179–1186 (2008).
87. Yu, Y., Clippinger, A. J. & Alwine, J. C. Viral effects on metabolism: changes in glucose and glutamine utilization during human cytomegalovirus infection. *Trends Microbiol.* **19**, 360–367 (2011).
88. Geisler, J., Touma, J., Rahbar, A., Söderberg-Nauclér, C. & Vetvik, K. A review of the potential role of human cytomegalovirus (HCMV) infections in breast cancer carcinogenesis and abnormal immunity. *Cancers* **11**, 1842 (2019).
89. Aminzadeh-Gohari, S. et al. Targeting mitochondria in melanoma. *Biomolecules* **10**, 1395 (2020).
90. Vincent, K. M. & Postovit, L. M. Investigating the utility of human melanoma cell lines as tumour models. *Oncotarget* **8**, 10498–10509 (2017).
91. Hargadon, K. M. Melanoma: methods and protocols. In *Methods in Molecular Biology*. 73–80 (Humana Press, 2021).
92. Desai, S. P., Bhatia, S. N., Toner, M. & Irimia, D. Mitochondrial localization and the persistent migration of epithelial cancer cells. *Biophys. J.* **104**, 2077–2088 (2013).
93. Jung, J. U. et al. NIK/MAP3K14 regulates mitochondrial dynamics and trafficking to promote cell invasion. *Curr. Biol.* **26**, 3288–3302 (2016).
94. Cai, Q. & Sheng, Z. H. Moving or stopping mitochondria: miro as a traffic cop by sensing calcium. *Neuron* **61**, 493–496 (2009).
95. Morlino, G. et al. Miro-1 links mitochondria and microtubule dynein motors to control lymphocyte migration and polarity. *Mol. Cell. Biol.* **34**, 1412–1426 (2014).
96. Castanier, C., Garcin, D., Vazquez, A. & Arnoult, D. Mitochondrial dynamics regulate the RIG-I-like receptor antiviral pathway. *EMBO Rep.* **11**, 133–138 (2010).
97. Jacobs, J. L. & Coyne, C. B. Mechanisms of MAVS regulation at the mitochondrial membrane. *J. Mol. Biol.* **425**, 5009–5019 (2013).
98. Hanada, Y. et al. MAVS is energized by Mff which senses mitochondrial metabolism via AMPK for acute antiviral immunity. *Nat. Commun.* **11**, 1–14 (2020).
99. Youle, R. J. & Narendra, D. P. Mechanisms of mitophagy. *Nat. Rev. Mol. Cell Biol.* **12**, 9–14 (2011).
100. Um, J. H. & Yun, J. Emerging role of mitophagy in human diseases and physiology. *BMB Rep.* **50**, 299 (2017).
101. Trifunovic, A. & Larsson, N. G. Mitochondrial dysfunction as a cause of ageing. *J. Intern. Med.* **263**, 167–178 (2008).
102. Munger, J., Bajad, S. U., Collier, H. A., Shenk, T. & Rabinowitz, J. D. Dynamics of the cellular metabolome during human cytomegalovirus infection. *PLoS Pathog.* **2**, 1165–1175 (2006).
103. Paradies, G., Paradies, V., De Benedictis, V., Ruggiero, F. M. & Petrosillo, G. Functional role of cardiolipin in mitochondrial bioenergetics. *Biochimica et Biophysica Acta - Bioenerg.* **1837**, 408–417 (2014).
104. Yu, D., Silva, M. C. & Shenk, T. Functional map of human cytomegalovirus AD169 defined by global mutational analysis. *Proc. Natl. Acad. Sci. USA* **100**, 12396–12401 (2003).
105. Yu, D., Smith, G. A., Enquist, L. W. & Shenk, T. Construction of a self-excisable bacterial artificial chromosome containing the human cytomegalovirus genome and mutagenesis of the diploid TRL/IRL13 gene. *J. Virol.* **76**, 2316–2328 (2002).
106. Schmidt, R. et al. Mitochondrial cristae revealed with focused light. *Nano Lett.* **9**, 2508–2510 (2009).
107. Kondadi, A. K., Anand, R. & Reichert, A. S. Cristae membrane dynamics—a paradigm change. *Trends Cell Biol.* **30**, 1–14 (2020).
108. Hagen, W. J. H., Wan, W. & Briggs, J. A. G. Implementation of a cryo-electron tomography tilt-scheme optimized for high resolution subtomogram averaging. *J. Struct. Biol.* **197**, 191–198 (2017).
109. Mastronarde, D. N. SerialEM: a program for automated tilt series acquisition on Tecnai microscopes using prediction of specimen position. *Microsc. Microanal.* **9**, 1182–1183 (2003).
110. Mastronarde, D. N. & Held, S. R. Automated tilt series alignment and tomographic reconstruction in IMOD. *J. Struct. Biol.* **197**, 102–113 (2017).
111. Demichev, V., Messner, C. B., Vernardis, S. I., Lilley, K. S. & Ralser, M. DIA-NN: neural networks and interference correction enable deep proteome coverage in high throughput. *Nat. Methods* **17**, 41–44 (2020).

Acknowledgements

The authors would like to thank Dr. Gary Laevsky and Dr. Sha Wang from the Princeton Confocal Core for the use of their instruments and their technical advice. The authors would also like to thank Dr. Todd Greco and Dr. Josiah Hutton for their advice on proteomics experiments. We also thank Dr. Yibin Kang and Dr. Mark Esposito for their generous gift of the A375 and HTB-140 melanoma cells. The authors would also like to thank the Wallace lab for their gift of the FRB-FKBP mito-mito tethering plasmids. The authors would also like to thank Dr. Joshua Rabinowitz for his insight. The authors also acknowledge support by Carolin Seuring, Cornelia Cazey and Ulrike Laugks for access to the Cryo-EM multi-user facility at CSSB and providing time for sample preparation, screening, and data collection; Wolfgang Lugmayr for help and support in using the CSSB partition on the DESY computer cluster for cryo-EM data processing. This work was funded by the National Institute of Health (NIH) (F31AI147637, K.C.C. & T32GM007388, K.C.C., W.A.H.), National Institute of Allergy and Infectious Disease (NIAID) (R01AI174515, I.M.C.), National Institute of General Medical Science (NIGMS) (R01GM114141, I.M.C.), American Heart Association (AHA) (23PRE1014367, WAH), National Science Foundation (NSF) (2021316158, JWP), Stand up to Cancer (SU2C) (3.1416, I.M.C.), Deutsche Forschungsgemeinschaft (DFG) (152/772-1; 152/774-1; 152/775-1; 152/776-1, K.G.) and the Klaus Tschira Boost Fund KT-33 (E.Q.).

Author contributions

This work was conceptualized by W.A.H., K.C.C., E.T., and I.M.C. W.A.H., K.C.C., E.Q., K.G., I.M.C., V.P., E.A.M., and J.W.P. developed the methodology and discussed the results. All experiments were performed by W.A.H., K.C.C., E.T., E.Q., R.G., and J.W.P. The manuscript was written by W.A.H. and edited by W.A.H., I.M.C., E.Q., K.G., V.P., and E.A.M.

Competing interests

The authors declare no competing interests.

Additional information

Supplementary information The online version contains supplementary material available at <https://doi.org/10.1038/s41467-024-51680-4>.

Correspondence and requests for materials should be addressed to Ileana M. Cristea.

Peer review information *Nature Communications* thanks Michael Weekes who co-reviewed with Joanne KiteLuca Scorrano and the anonymous, reviewer(s) for their contribution to the peer review of this work. A peer review file is available.

Reprints and permissions information is available at <http://www.nature.com/reprints>

Publisher's note Springer Nature remains neutral with regard to jurisdictional claims in published maps and institutional affiliations.

Open Access This article is licensed under a Creative Commons Attribution-NonCommercial-NoDerivatives 4.0 International License, which permits any non-commercial use, sharing, distribution and reproduction in any medium or format, as long as you give appropriate credit to the original author(s) and the source, provide a link to the Creative Commons licence, and indicate if you modified the licensed material. You do not have permission under this licence to share adapted material derived from this article or parts of it. The images or other third party material in this article are included in the article's Creative Commons licence, unless indicated otherwise in a credit line to the material. If material is not included in the article's Creative Commons licence and your intended use is not permitted by statutory regulation or exceeds the permitted use, you will need to obtain permission directly from the copyright holder. To view a copy of this licence, visit <http://creativecommons.org/licenses/by-nc-nd/4.0/>.

© The Author(s) 2024

¹Department of Molecular Biology, Princeton University, Princeton, NJ, USA. ²Department of Chemistry, MIN Faculty, Universität Hamburg, Hamburg, Germany. ³Department of Structural Cell Biology of Viruses, Centre for Structural Systems Biology, Leibniz Institute of Virology, Hamburg, Germany. ⁴Department of Virology, Institute for Integrative Biology of the Cell, CNRS UMR9198, Gif-sur-Yvette, France.

✉ e-mail: icristea@princeton.edu